SIAM J. APPL. MATH.
Vol. 86, No. 3, pp. 919–944

ANALYZING THE NEMATIC LIQUID CRYSTAL DROPLET WITH AN IMPROVED DIFFUSE-INTERFACE LANDAU–DE GENNES MODEL*

BAOMING SHI†, DAWEI WU†, LEI ZHANG‡, AND PINGWEN ZHANG§

Abstract. The nematic liquid crystal droplet problem is of significant interest due to the complex interplay between variable droplet shapes and orientation fields, with numerous applications in physics and material science. Here we introduce an improved diffuse-interface Landau–de Gennes model for nematic liquid crystal droplets, which eliminates an artificial penalty term from [Wu et al., *SIAM J. Math. Anal.*, 57 (2025), pp. 4358–4395] that is inconsistent with the classical droplet problem. We prove the existence of minimizers and Γ-convergence to a physically interpretable sharp-interface energy functional. We also present asymptotic solutions across the interface between the interior nematic droplet and external isotropic phase. Numerical simulations reveal optimal droplet configurations—radial, ring, and tactoid—highlighting the mutual influence between topological defects and droplet morphology. Furthermore, we construct a phase diagram of (meta)stable configurations as a function of temperature and domain size, delineating distinct stability regimes for biaxial and uniaxial phases.

Key words. Landau–de Gennes model, nematic liquid crystals, diffuse interface, phase field, free boundary, asymptotic analysis

MSC codes. 76A15, 49J27, 49J45, 34E05

DOI. 10.1137/25M1764864

1. Introduction.

Liquid crystals (LCs) represent a state of matter intermediate between solids and liquids [6]. Among them, *nematic liquid crystals* (NLCs) are the simplest and most widely used in both scientific research and technological applications. NLCs exhibit long-range orientational order, characterized by one or more preferred directions of molecular alignment, commonly referred to as nematic *directors.* As a result, NLCs display anisotropic physical, optical, and rheological properties [51]. NLC *droplets* are finite regions of NLCs in three-dimensional (3D) space, bounded by free interfaces shaped by the interplay of surface tension and anisotropic molecular alignment. These droplets exhibit distinctive physical behaviors and are integral to applications such as liquid crystal displays [9, 29, 52, 64, 69]. Furthermore, the study of NLC droplets offers insights into the broader classes of anisotropic materials [32, 36, 48].

The practical applications of NLC droplets have spurred extensive mathematical investigation [1, 8, 15, 67, 22, 27, 33, 37, 68]. An effective and accurate model for NLC droplets must address two central challenges: (1) capturing the nematic orientation

*Received by the editors June 2, 2025; accepted for publication (in revised form) December 1, 2025; published electronically May 8, 2026.
https://doi.org/10.1137/25M1764864
Funding: This work was supported by the National Natural Science Foundation of China (grants 12225102, T2321001, 12288101, and 12426653).
†School of Mathematical Sciences, Peking University, Beijing 100871, China (ming123@stu.pku.edu.cn, 2201110052@pku.edu.cn).
‡School of Mathematical Sciences, Beijing International Center for Mathematical Research, Center for Quantitative Biology, Center for Machine Learning Research, Peking University, Beijing 100871, China (zhangl@math.pku.edu.cn).
§School of Mathematics and Statistics, Wuhan University, Wuhan 430072, China, and School of Mathematical Sciences, Peking University, Beijing 100871, China (pzhang@pku.edu.cn).

within the droplet, and (2) determining the optimal droplet shape. Popular models of the droplet shape include the sharp-interface surface mesh method [3], which discretizes the free boundary using a finite element mesh, and the diffuse-interface method [62] that employs a smooth phase field to represent phase separation and interfacial regions. To model nematic orientation, several frameworks are available: the microscopic Onsager model [45], the macroscopic Oseen–Frank (OF) model [16, 46], and the Landau–de Gennes (LdG) model that describes the NLC phase using a **Q**-tensor order parameter [23, 61].

By combining a description of the droplet shape with a model for the internal nematic orientation, one obtains a complete formulation of the NLC droplet problem. For example, using a sharp-interface representation for the droplet boundary together with either the OF or the LdG model for the nematic order parameter, the problem can be posed as the following variational minimization [10, 34, 58, 59].

PROBLEM A. *Find an order parameter field* $\mathbf{X}^*$ *and a shape* $A^* \subset \mathbb{R}^3$ *minimizing*

$$\mathscr{F}[\mathbf{X}, A] = \int_A W(\mathbf{X}, \boldsymbol{\nabla}\mathbf{X})\,\mathrm{d}x + \int_{\partial A} F_a(\mathbf{X}, \boldsymbol{\nu})\,\mathrm{d}S \tag{1.1}$$

subject to the volume constraint $|A| = V_0$*. Here,* W *denotes the bulk free energy density associated with the nematic order parameter* $\mathbf{X}$*, and* F_a *is a surface anchoring energy that encodes preferred alignments between the nematic director(s) and the outward unit normal vector* $\boldsymbol{\nu}$ *on* ∂A*.*

A particular class of droplet shapes, known as *tactoids,* has been frequently observed in experiments [43, 56, 55, 60, 54]. Tactoids are spindle-shaped, with a prolate geometry and pointed ends. Their formation has also been studied theoretically [66, 58, 27, 18] and numerically [68, 8, 1]. For instance, in [58], the author examines the emergence of spindle-shaped tactoids through a construction based on Wulff's conjecture. In [1], a deformable two-dimensional (2D) nematic liquid crystal confinement is modelled using a finite element mesh. The numerical results show that, under sufficiently strong Dirichlet boundary conditions, the optimal droplet shape approaches a tactoid, in agreement with experimental observations. In [68], a diffuse-interface model is employed, where a phase field ϕ represents the separation between a nematic liquid crystal and a Newtonian fluid. Energy minimization within this framework yields a slightly prolate spheroidal droplet.

There are two primary issues with the existing models: (1) the inability of the vector-based model to describe biaxiality and certain topological defects, and (2) computational inefficiency. Regarding the first issue, most approaches to the NLC droplet problem employ the vector model [8, 22, 67]. However, the vector order parameter $\mathbf{n}$ fails to represent certain topological defects. For example, the $+1$ defect results in an infinite energy within the OF model in 2D. Additionally, fractional defects, such as $\pm 1/2$ defects where the director overlaps with itself after a 180-degree rotation, cannot be continuously represented by the vector model. As for the second issue, some implementations of deformable shapes utilize the finite element method [1, 8]. While the finite element method accurately captures irregular shapes, it is computationally inefficient and unable to model topological changes, such as droplet splitting or merging, because the mesh is topologically invariant.

To address these challenges, we have recently proposed a diffuse-interface energy functional for the 3D NLC droplet problem [65]. This functional used the LdG model coupled with a phase field function. The LdG theory accommodates both uniaxial and biaxial NLC phases with spatially varying orientational order and can represent

topological defects of various dimensionalities. We adopted the diffuse-interface model [5, 17, 68] to describe the deformable shape for computational efficiency. We also proved that the diffuse-interface energy functional Γ-converges to a sharp-interface functional of the following form:

$$E_0 = \int_A E^{\mathrm{LdG}}\,\mathrm{d}x + \int_{\partial A} E^{\mathrm{anch}}\,\mathrm{d}S + \int_{A^c} E^{\mathrm{void}}\,\mathrm{d}x, \tag{1.2}$$

where A denotes the region occupied by the droplet. However, the sharp-interface functional obtained after the Γ-limit still contained an artificial penalty term E^{void} in the exterior of the droplet (denoted by A^c in (1.2)). In contrast, the desired droplet energy, as given by (1.1), integrates over the interior and surface of the droplet only. Consequently, the numerically obtained tactoids exhibited excessively rounded tips, a feature that deviated from experiments.

In this work, we introduce an improved diffuse-interface LdG energy functional that, upon taking the sharp-interface limit, converges to a form consistent with the droplet energy functional (1.1). This refined energy functional retains several key properties from our previous formulation, such as the existence of minimizers. We also heuristically derive one-dimensional (1D) asymptotic solutions to the diffuse-interface energy and demonstrate that they lead to sharp phase separations across an infinitesimal interval, thereby confirming the consistency of our sharp-interface limit. Numerically, we identify multiple (meta)stable configurations within the diffuse-interface energy. Along with the expected spindle-shaped tactoids, we discover spherical radial and oblate spheroidal ring configurations in small domains—configurations that cannot be predicted by the vector models in [67, 8, 22]. We explore the mutual influence between topological defects and droplet shapes: defects tend to push the nearest boundary outward, as observed in the ring configuration, while sharp angles at the boundary can eliminate defects, as seen in the spindle-shaped tactoids. Furthermore, we investigate the structural transitions of stable droplet configurations as functions of temperature and domain size.

The rest of the paper is organized as follows: the energy functional is given in section 2; proofs of the existence of minimizers and the sharp-interface limit are given in section 3; asymptotic solutions are explained in section 4; numerical results are discussed in section 5.

2. Modelling. We study an NLC droplet in 3D periodic space $\Omega = \mathbb{T}^3$, which is parametrized by the unit cube $[0,1]^3$. The periodic setting describes an infinite 3D array of identical droplets that occupy the entire Euclidean space, which is similar to the experimental setting in [28]. We have two order parameters: $\mathbf{Q}$ is the order parameter for nematic orientation, which is a symmetric traceless tensor, and ϕ is the order parameter for the interface. We refer to the pair $(\mathbf{Q}, \phi)$ as a configuration. The diffuse-interface LdG energy is then defined as

$$\begin{aligned}\mathscr{E}_{\varepsilon,\kappa}(\mathbf{Q},\phi) = &\int_\Omega \phi^2 \left[\frac{1}{2\lambda}|\boldsymbol{\nabla}\mathbf{Q}|^2 + \lambda\left(\frac{a}{2}\operatorname{tr}\mathbf{Q}^2 - \frac{b}{3}\operatorname{tr}\mathbf{Q}^3 + \frac{1}{4}(\operatorname{tr}\mathbf{Q}^2)^2 - B_{\min}\right)\right]\mathrm{d}x\\ &+ w_p\int_\Omega \left[\varepsilon^{-1}\phi^2(1-\phi)^2 + \varepsilon|\nabla\phi|^2 + \omega\varepsilon\left|\left(\mathbf{Q} + \frac{s_+}{3}\mathbf{I}\right)\nabla\phi\right|^2\right]\mathrm{d}x\\ &+ \frac{w_v}{2}\int_\Omega \left[\kappa|\boldsymbol{\nabla}\mathbf{Q}|^2 + \kappa^{-1}(1-\phi)^2|\mathbf{Q}|^2\right]\mathrm{d}x,\end{aligned} \tag{2.1}$$

subject to the volume constraint

$$\int_\Omega \phi \, \mathrm{d}x = V_0, \tag{2.2}$$

where $a, b, B_{\min}, s_+$ are physical constants ($B_{\min}$ and s_+ are determined by a and b), λ is proportional to the domain size, $\varepsilon, \kappa > 0$ are small numbers, and $w_p, w_v, \omega > 0$ are positive weights. $\mathscr{E}_{\varepsilon,\kappa}$ consists of a volume integral of the LdG free energy density inside the droplet, a diffuse-interface surface energy in Van der Waals–Cahn–Hilliard form [57, 4] that takes into account the anchoring effect, and a penalty term outside the droplet.

Landau–de Gennes energy. Recall that the spatial region A occupied by the NLC droplet is approximated by ϕ, where $\phi(x) = 1$ indicates $x \in A$ and $\phi(x) = 0$ indicates that $x \in A^c$. Hence, the first term of our energy (2.1) is the LdG free energy [6, 41, 61] in the region A:

$$E^{\mathrm{LdG}} = \int_\Omega \phi^2 \left[\frac{1}{2\lambda} |\boldsymbol{\nabla} \mathbf{Q}|^2 + \lambda \bar{F}_b(\mathbf{Q}) \right] \mathrm{d}x. \tag{2.3}$$

The order parameter in the LdG model is a symmetric traceless tensor

$$\mathbf{Q} = ((Q^{ij}))_{3\times 3} \in \mathcal{S}_0 = \{\mathbf{A} \in \mathbb{R}^{3\times 3} : \mathbf{A} = \mathbf{A}^T, \operatorname{tr} \mathbf{A} = 0\}. \tag{2.4}$$

The eigenvector of $\mathbf{Q}$ with the maximum eigenvalue represents the nematic director. A $\mathbf{Q}$-tensor is said to be isotropic if $\mathbf{Q} = \mathbf{0}$, uniaxial if $\mathbf{Q}$ has a pair of repeated nonzero eigenvalues, and biaxial if $\mathbf{Q}$ has three distinct eigenvalues [41]. A uniaxial NLC phase has a single distinguished direction of averaged molecular alignment (modelled by the eigenvector with the nondegenerate eigenvalue), such that all directions perpendicular to the uniaxial director are physically equivalent. A biaxial phase has a primary and a secondary nematic director.

The LdG free energy density in (2.3) is a combination $\lambda^{-1}\bar{F}_{el} + \lambda \bar{F}_b$, where the first term in the integrand,

$$\bar{F}_{el}(\mathbf{Q}) = \frac{1}{2} |\boldsymbol{\nabla} \mathbf{Q}|^2 = \frac{1}{2} \sum_{i,j,k} |Q^{ij}_k|^2, \tag{2.5}$$

is the elastic energy density that penalizes spatial inhomogeneities, and the second term in the integrand,

$$\bar{F}_b(\mathbf{Q}) = \frac{a}{2} \operatorname{tr} \mathbf{Q}^2 - \frac{b}{3} \operatorname{tr} \mathbf{Q}^3 + \frac{1}{4} (\operatorname{tr} \mathbf{Q}^2)^2 - B_{\min}, \tag{2.6}$$

is the bulk energy density with a temperature-related constant a and a material constant b. $B_{\min} = \min_{\mathbf{Q}\in\mathcal{S}_0} \bar{F}_b$ is a constant subtracted from the bulk energy density to ensure positivity. Minimizers of $\bar{F}_b$ depend on a, b and determine the NLC phase for spatially homogeneous samples. For $a < \frac{b^2}{27}$ (i.e., low temperature), these minimizers constitute a continuum of uniaxial $\mathbf{Q}$-tensors defined by

$$\mathcal{N} = \left\{ \mathbf{Q} = s_+ \left(\mathbf{n} \otimes \mathbf{n} - \frac{1}{3} \mathbf{I} \right) \right\}, \tag{2.7}$$

where

$$s_+ = \frac{b + \sqrt{b^2 - 24a}}{4} \tag{2.8}$$

and $\mathbf{n}$ is an arbitrary unit vector that models the uniaxial director.

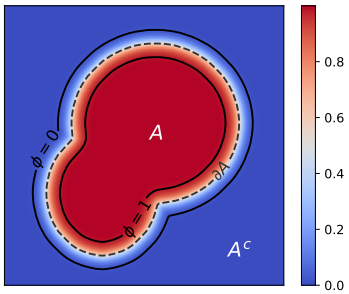

FIG. 2.1. *Illustration of the phase field. As color changes from red to blue, phase changes from nematic ($\phi = 1$) to isotropic ($\phi = 0$) via a diffuse interface with thickness $O(\varepsilon)$ surrounding the surface ∂A. (Color figure available online.)*

Mixing energy. The second integral from our energy (2.1) is the mixing energy, which constrains the smoothness of the droplet interface as well as the planar (tangent) anchoring of NLC molecules. The mixing energy is given by

$$E^{\text{mix}} = w_p \int_\Omega \left[\varepsilon^{-1}\phi^2(1-\phi)^2 + \varepsilon|\nabla\phi|^2 + \omega\varepsilon \left| \left(\mathbf{Q} + \frac{s_+}{3}\mathbf{I} \right) \nabla\phi \right|^2 \right] \mathrm{d}x, \tag{2.9}$$

where ε represents the thickness of the diffuse interface (sometimes termed the "capillary width" [68]) and $w_p > 0$ is an adjustable weight. The term $\varepsilon^{-1}\phi^2(1-\phi)^2$ prefers that ϕ equals 0 or 1 constantly, while the term $\varepsilon|\nabla\phi|^2$ retains its smoothness. As a result, ϕ represents a smoothed-out phase separation: ϕ equals the constant 0 or 1 in the majority of the domain and changes rapidly within a diffuse interface where its gradient $\nabla\phi$ points in the normal direction, as illustrated in Figure 2.1. The coefficients ε^{-1} and ε scale the integral to $O(1)$.

The function

$$f_a(\mathbf{Q}, \boldsymbol{\nu}) = \left| \left(\mathbf{Q} + \frac{s_+}{3}\mathbf{I} \right) \boldsymbol{\nu} \right|^2, \tag{2.10}$$

with a positive weight ω, is a weak anchoring energy that penalizes the misalignment between $\mathbf{Q}$ and the direction $\boldsymbol{\nu}$ [25, 49], which we take to be the normal direction to the interface characterized by $\nabla\phi \approx O(\varepsilon^{-1}) \cdot \boldsymbol{\nu}$. The penalty f_a vanishes when ν is an eigenvector of $\mathbf{Q}$ with eigenvalue $-s_+/3$, that is, the leading nematic director (eigenvector of $\mathbf{Q}$ with the largest eigenvalue) is orthogonal to ν, and the nematic director is tangential to the interface. In particular, f_a vanishes when $\mathbf{Q}$ is the uniaxial minimizer (2.7) with $\mathbf{n} \perp \nu$.

Remark 2.1. The first two terms in our mixing energy (2.9) are the famous Van der Waals-Cahn-Hilliard functional [4]

$$F_\varepsilon[u] = \int_\Omega [\varepsilon^{-1}W(u) + \varepsilon|\nabla u|^2] \, \mathrm{d}x. \tag{2.11}$$

It models two-phase mixtures in physics and has been proved to Γ-converge to the interface perimeter functional when $\varepsilon \to 0$ [39, 53].

Void penalty. The third integral from (2.1) is the void penalty, which constrains the exterior phase to be isotropic. The void penalty is given by

$$E^{\text{void}} = \frac{w_v}{2} \int_\Omega [\kappa|\boldsymbol{\nabla}\mathbf{Q}|^2 + \kappa^{-1}(1-\phi)^2|\mathbf{Q}|^2] \, \mathrm{d}x, \tag{2.12}$$

TABLE 2.1
Parameters of the energy functional (2.1).

Parameter	Meaning
λ	Characteristic scale, proportional to domain size
a, b	Physical parameters of the LdG bulk energy $\bar{F}_b(\mathbf{Q})$
$B_{\min}$	Minimum of $\bar{F}_b$, determined by a, b
s_+	Scalar order parameter such that $\mathbf{Q} = s_+(\mathbf{n}\otimes\mathbf{n} - \frac{1}{3}\mathbf{I})$ minimizes $\bar{F}_b$, determined by a, b
w_p	Weight of the mixing energy
w_v	Weight of the void penalty
ε	Capillary width of ϕ, represents thickness of ϕ-interface
ω	Strength of weak anchoring
κ	Capillary width of $\mathbf{Q}$, represents thickness of $\mathbf{Q}$-interface

where $|\mathbf{Q}|^2 = \operatorname{tr}\mathbf{Q}^2 = \sum_{i,j}|Q^{ij}|^2$, $w_v > 0$ is an adjustable weight, and $\kappa > 0$ is another capillary width representing the thickness of the diffuse interface for $\mathbf{Q}$, similar to ε in (2.9). The $|\boldsymbol{\nabla}\mathbf{Q}|^2$ term ensures the overall coercivity of $\mathscr{E}_{\varepsilon,\kappa}$ with respect to $\mathbf{Q}$, and the $(1-\phi)^2|\mathbf{Q}|^2$ term restricts the integration to the isotropic region $\phi = 0$, imposing that $\mathbf{Q} \equiv 0$ in the isotropic region.

In summary, the energy functional (2.1) is composed of an LdG energy restricted to the droplet $\phi = 1$, a mixing energy with weak anchoring, and a void penalty enforcing that $\mathbf{Q} = 0$ when $\phi = 0$. The model contains many parameters, a glossary of which can be found in Table 2.1.

3. Existence and Γ-convergence. In this section, we discuss the existence of minimizers and the Γ-convergence to a sharp-interface limit. The admissible $(\mathbf{Q}, \phi)$ belong to the space

$$\mathscr{A} = \left\{ (\mathbf{Q}, \phi) : \mathbf{Q} \in H^1(\Omega; \mathcal{S}_0), \phi \in H^1(\Omega), \int_\Omega \phi \,\mathrm{d}x = V_0 \right\}, \tag{3.1}$$

where $H^1(\Omega)$ is the Sobolev space with periodic boundary conditions,

$$H^1(\Omega) = \left\{ u \in L^2(\Omega) : \int_\Omega |\nabla u|^2 \,\mathrm{d}x < \infty \right\}, \tag{3.2}$$

and

$$H^1(\Omega; \mathcal{S}_0) = \{ \mathbf{Q} \in L^2(\Omega, \mathcal{S}_0) : \mathbf{Q} \in H^1(\Omega) \} \tag{3.3}$$

is the collection of H^1 mappings that take values in $\mathcal{S}_0$, the space of symmetric traceless matrices.

3.1. Properties of the minimizers. We first prove the existence of minimizers of (2.1).

PROPOSITION 3.1. *For any set of positive parameters* $(a, b, \lambda, V_0, \varepsilon, \kappa, \omega, w_p, w_v)$, *there exists a minimizer* $(\mathbf{Q}^*, \phi^*) \in \mathscr{A}$ *such that*

$$\mathscr{E}_{\varepsilon,\kappa}[\mathbf{Q}^*, \phi^*] = \inf_{(\mathbf{Q},\phi)\in\mathscr{A}} \mathscr{E}_{\varepsilon,\kappa}[\mathbf{Q}, \phi].$$

Proof. We only need to verify the weak lower-semicontinuity (w.l.s.c.) and coercivity of the functional.

Note that the linear constraint (2.2) on ϕ required by $\mathscr{A}$ is a continuous functional in $H^1(\Omega)$, so $\mathscr{A}$ is a weakly closed submanifold of $H^1(\Omega)$. Hence, for the w.l.s.c. of $\mathscr{E}_{\varepsilon,\kappa}$ on $\mathscr{A}$, we only need to verify w.l.s.c. on the entire space $H^1(\Omega; \mathcal{S}_0) \times H^1(\Omega)$. We notice that the energy can be written as

$$\mathscr{E}_{\varepsilon,\kappa} = E_1(\boldsymbol{\nabla}\mathbf{Q},\phi) + E_2(\nabla\phi,\mathbf{Q}) + E_3(\mathbf{Q},\phi), \tag{3.4}$$

where we temporarily denote

$$E_1 = \int_\Omega \frac{1}{2}\left(\frac{\phi^2}{\lambda} + w_v\kappa\right)|\boldsymbol{\nabla}\mathbf{Q}|^2\,\mathrm{d}x, \tag{3.5a}$$

$$E_2 = w_p\varepsilon\int_\Omega \nabla\phi\cdot\left[\mathbf{I} + \omega\left(\mathbf{Q} + \frac{s_+}{3}\mathbf{I}\right)^2\right]\nabla\phi\,\mathrm{d}x, \tag{3.5b}$$

$$E_3 = \int_\Omega \left[\lambda\phi^2\bar{F}_b(\mathbf{Q}) + \frac{w_p}{\varepsilon}\phi^2(1-\phi)^2 + \frac{w_v}{2\kappa}(1-\phi)^2|\mathbf{Q}|^2\right]\mathrm{d}x. \tag{3.5c}$$

As the integrand of E_1 is a positive quadratic form (which is convex) with respect to $\boldsymbol{\nabla}\mathbf{Q}$ and continuous in ϕ, according to [11, Chapter 8, Thm. 1], whose reasoning also applies in the periodic setting here, E_1 has w.l.s.c. Similarly, the integrand of E_2 is positive, convex in $\nabla\phi$, and continuous in $\mathbf{Q}$, while that of E_3 is also positive and depends entirely on $\mathbf{Q},\phi$, so similar reasoning applies, and they also have w.l.s.c. Consequently, their sum $\mathscr{E}_{\varepsilon,\kappa}$ has w.l.s.c.

For coercivity, we also verify that $\mathscr{E}_{\varepsilon,\kappa}\to\infty$ as $\|\mathbf{Q}\|_{H^1} + \|\phi\|_{H^1}\to\infty$ on the entire space $H^1(\Omega;\mathcal{S}_0)\times H^1(\Omega)$. We notice that the LdG bulk energy (2.6) satisfies

$$\bar{F}_b(\mathbf{Q}) \geq c_1|\mathbf{Q}|^2 - c_2 \tag{3.6}$$

where c_1, c_2 are constants, because F_b is a 4th-degree polynomial in $\mathbf{Q}$. Similarly, the double-well potential satisfies that $\frac{w_p}{\varepsilon}W(\phi)\geq c_4\phi^2 - c_5$. Combining the estimates for $\bar{F}_b$ and $W(\phi)$ with the void penalty (2.12), we get

$$\begin{aligned}\lambda\phi^2\bar{F}_b(\mathbf{Q}) + \frac{w_p}{\varepsilon}W(\phi) + \frac{w_v}{2\kappa}(1-\phi)^2|\mathbf{Q}|^2 &\geq 4c_3(\phi^2 + (1-\phi)^2)|\mathbf{Q}|^2 + c_4\phi^2 - c_5\\ &\geq c_3|\mathbf{Q}|^2 + c_4\phi^2 - c_5,\end{aligned} \tag{3.7}$$

where c_3 is an appropriate positive constant related to the model parameters and c_1, c_2. Then, we find that $\mathscr{E}_{\varepsilon,\kappa}$ satisfies

$$\begin{aligned}\mathscr{E}_{\varepsilon,\kappa} &\geq \int_\Omega \left[\frac{w_v\kappa}{2}|\boldsymbol{\nabla}\mathbf{Q}|^2 + w_p\varepsilon|\nabla\phi|^2 + c_3|\mathbf{Q}|^2 + c_4\phi^2 - c_5\right]\mathrm{d}x\\ &\geq \frac{1}{K}(\|\mathbf{Q}\|^2_{H^1(\Omega)} + \|\phi\|^2_{H^1(\Omega)}) - c_5,\end{aligned} \tag{3.8}$$

where K is a constant related to model parameters. Therefore, $\mathscr{E}_{\varepsilon,\kappa}$ is coercive on the entire space, and also coercive on the constrained manifold $\mathscr{A}$.

The rest of the derivation is standard. Coercivity implies that $\mathscr{E}_{\varepsilon,\kappa}$ is bounded below on $\mathscr{A}$, so there exists a sequence $\{(\mathbf{Q}_n,\phi_n)\}\subset\mathscr{A}$ such that

$$\mathscr{E}_{\varepsilon,\kappa}[\mathbf{Q}_n,\phi_n]\to\inf_{\mathscr{A}}\mathscr{E}_{\varepsilon,\kappa}. \tag{3.9}$$

$(\mathbf{Q}_n,\phi_n)$ must be bounded under the H^1 norm, so by the weak compactness of the H^1 space, it has a weakly convergent subsequence. Without loss of generality, we regard $\{(\mathbf{Q}_n,\phi_n)\}$ as the weakly convergent subsequence; then its weak limit $(\mathbf{Q}^*,\phi^*)$ must belong to $\mathscr{A}$ due to the weak closedness of $\mathscr{A}$, and by w.l.s.c. we have that

$$\mathscr{E}_{\varepsilon,\kappa}[\mathbf{Q}^*,\phi^*]\leq\liminf_{n\to\infty}\mathscr{E}_{\varepsilon,\kappa}[\mathbf{Q}_n,\phi_n] = \inf_{\mathscr{A}}\mathscr{E}_{\varepsilon,\kappa}, \tag{3.10}$$

which completes our proof. ∎

3.2. Sharp-interface limit. We prove that when ε, κ tend to 0, the energy $\mathscr{E}_{\varepsilon,\kappa}$ (2.1) converges to a sharp-interface energy of the form (1.1) in the sense of De Giorgi's Γ-convergence [7], which indicates that if the minimizers of an array of functions converge to some limit, then the bespoke limit point is a minimizer of the limiting functional. In our case, the Γ-convergence of $\mathscr{E}_{\varepsilon,\kappa}$ indicates that the diffuse-interface energy functional can approximate a sharp-interface functional with small ε, κ.

LEMMA 3.2 ([2, Props. 4.1 and 4.2]). *Define the functional*

$$F_\varepsilon(u) = \frac{1}{\varepsilon}\int_{\Omega_0} f(x, u, \varepsilon\nabla u)\,\mathrm{d}x \tag{3.11}$$

where $\Omega_0 \subset \mathbb{R}^n$ is a Lipschitz domain and $f(x,u,p) : \Omega_0 \times \mathbb{R} \times \mathbb{R}^n \to \mathbb{R}$ is a continuous function that satisfies the following:

(i) *For all $x \in \Omega_0$, $f(x,\cdot,0)$ is a double-well function, i.e., it has strict minima at $u = \alpha(x), \beta(x)$ $(\alpha(x) \le \beta(x))$.*
(ii) *For all $(x,u) \in \Omega_0 \times \mathbb{R}$, $f(x,u,\cdot)$ is convex in $p \in \mathbb{R}^n$ and differentiable at $p = 0$ where it achieves a strict minimum.*
(iii) *There exists $\Phi(t) : \mathbb{R}_+ \to \mathbb{R}_+$ such that $\lim_{t\to\infty} \Phi(t)/t = \infty$ and $f(x,u,0) > \Phi(|u|)$.*

Then, the Γ-limit of the energy functional $F_\varepsilon(u)$ under L^1 strong topology as $\varepsilon \to 0$ and $u_\varepsilon \to u$ subject to the volume constraint

$$\int_{\Omega_0} u_\varepsilon\,\mathrm{d}x = m \quad \forall\varepsilon \tag{3.12}$$

is

$$F_0(A) = \int_{\partial^* A \cap \Omega_0} h(x, \boldsymbol{\nu}_A)\,\mathrm{d}S, \tag{3.13}$$

where u satisfies that $u(x) \in \{\alpha(x), \beta(x)\}$ a.e., $A = \{x, u = \alpha(x)\}$ is a region in Ω_0, $\partial^* A$ is the reduced boundary [21], $\boldsymbol{\nu}_A$ is the exterior normal vector, and $h(x,p)$ is defined as

$$h(x,p) = \int_{\alpha(x)}^{\beta(x)} \inf_{t>0}\left[\frac{1}{t} f(x,s,tp)\right]\mathrm{d}s. \tag{3.14}$$

A Γ-limit from F_ε to F_0 under the L^1 topology means that

(a) *for all sequences $u_\varepsilon \to u_0$ in L^1 where $u_0(x) = \alpha(x) I_A(x) + \beta(x) I_{A^c}(x)$,*

$$\liminf_{\varepsilon\to 0} F_\varepsilon(u_\varepsilon) \ge F_0(u_0); \tag{3.15}$$

(b) *there exists a sequence $u_\varepsilon \to u_0$ in L^1, such that*

$$\limsup_{\varepsilon\to 0} F_\varepsilon(u_\varepsilon) \le F_0(u_0) \tag{3.16}$$

and that $\alpha(x) \le u_\varepsilon \le \beta(x)$ everywhere.

We state our Γ-limit as $\varepsilon \to 0$ first in the following proposition.

PROPOSITION 3.3. *Suppose that $A \subset \Omega = \mathbb{T}^3$ is a C^2 region satisfying the volume constraint $|A| = V_0$ and that $\mathbf{Q} \in C^0(\Omega) \cap H^1(\Omega)$. Let the anchoring energy f_a take the form* (2.10). *Define the following energy:*

$$\begin{aligned}\mathscr{E}_{0,\kappa}[\mathbf{Q},A] &= \int_A \left[\frac{1}{2\lambda}|\boldsymbol{\nabla}\mathbf{Q}|^2 + \frac{w_v\kappa}{2}|\boldsymbol{\nabla}\mathbf{Q}|^2 + \lambda\bar{F}_b(\mathbf{Q})\right]\mathrm{d}x \\ &\quad + 2c_0 w_p \int_{\partial A}\sqrt{1+\omega f_a(\mathbf{Q},\boldsymbol{\nu})}\,\mathrm{d}S \\ &\quad + \frac{w_v}{2}\int_{A^c}\left[\kappa|\boldsymbol{\nabla}\mathbf{Q}|^2 + \kappa^{-1}|\mathbf{Q}|^2\right]\mathrm{d}x,\end{aligned} \tag{3.17}$$

where

$$c_0 = \int_0^1 \sqrt{W(s)}\,\mathrm{d}s \tag{3.18}$$

with $W(s) = s^2(1-s)^2$. *Then it holds that*

(a) *for any sequence* $\{\phi_\varepsilon\}$ *in* L^1 *such that* $\phi_\varepsilon \to I_A$ *in* L^1 *as* $\varepsilon \to 0$,

$$\liminf_{\varepsilon\to 0}\mathscr{E}_{\varepsilon,\kappa}[\mathbf{Q},\phi_\varepsilon] \geq \mathscr{E}_{0,\kappa}[\mathbf{Q},A]; \tag{3.19}$$

(b) *there exists a sequence* $\{\phi_\varepsilon\}$ *satisfying the constraint* (2.2), *with* $0 \leq \phi_\varepsilon \leq 1, \phi_\varepsilon \to I_A$ *in* L^1, *such that*

$$\lim_{\varepsilon\to 0}\mathscr{E}_{\varepsilon,\kappa}[\mathbf{Q},\phi_\varepsilon] = \mathscr{E}_{0,\kappa}[\mathbf{Q},A]. \tag{3.20}$$

Proof. By Fatou's lemma, for all sequences $\{\phi_\varepsilon\} \to I_A$ in $L^1(\Omega)$,

$$\liminf_{\varepsilon\to 0}\int_\Omega \phi^2\left[\frac{1}{2\lambda}|\boldsymbol{\nabla}\mathbf{Q}|^2 + \lambda\bar{F}_b(\mathbf{Q})\right]\mathrm{d}x \geq \int_A\left[\frac{1}{2\lambda}|\boldsymbol{\nabla}\mathbf{Q}|^2 + \lambda\bar{F}_b(\mathbf{Q})\right]\mathrm{d}x \tag{3.21}$$

and

$$\begin{aligned}&\liminf_{\varepsilon\to 0}\frac{w_v}{2}\int_\Omega\left[\kappa|\boldsymbol{\nabla}\mathbf{Q}|^2 + \kappa^{-1}(1-\phi)^2|\mathbf{Q}|^2\right]\mathrm{d}x \\ &\qquad \geq \int_A \frac{w_v\kappa}{2}|\boldsymbol{\nabla}\mathbf{Q}|^2\,\mathrm{d}x + \frac{w_v}{2}\int_{A^c}\left[\kappa|\boldsymbol{\nabla}\mathbf{Q}|^2 + \kappa^{-1}|\mathbf{Q}|^2\right]\mathrm{d}x,\end{aligned} \tag{3.22}$$

so conclusion (a) (the lower limit in (3.19)) holds for the LdG energy in (2.3) and the void penalty in (2.12). Moreover, suppose that there exists a sequence $\{\phi_\varepsilon\}$ satisfying the conditions of conclusion (b). Then, with a simple divide-and-conquer argument using partitions of the domain into sets $\{|\phi_\varepsilon - \phi| < \delta\}$ and $\{|\phi_\varepsilon - \phi| \geq \delta\}$, we can prove that the lower limits in (3.21) and (3.22) become the following equalities:

$$\begin{aligned}\lim_{\varepsilon\to 0}\int_\Omega \phi_\varepsilon^2\left[\frac{1}{2\lambda}|\boldsymbol{\nabla}\mathbf{Q}|^2 + \lambda\bar{F}_b(\mathbf{Q})\right]\mathrm{d}x &= \int_A\left[\frac{1}{2\lambda}|\boldsymbol{\nabla}\mathbf{Q}|^2 + \lambda\bar{F}_b(\mathbf{Q})\right]\mathrm{d}x, \\ \lim_{\varepsilon\to 0}\frac{w_v}{2}\int_\Omega\left[\kappa|\boldsymbol{\nabla}\mathbf{Q}|^2 + \kappa^{-1}(1-\phi_\varepsilon)^2|\mathbf{Q}|^2\right]\mathrm{d}x &= \int_A \frac{w_v\kappa}{2}|\boldsymbol{\nabla}\mathbf{Q}|^2\,\mathrm{d}x \\ &\quad + \frac{w_v}{2}\int_{A^c}\left[\kappa|\boldsymbol{\nabla}\mathbf{Q}|^2 + \kappa^{-1}|\mathbf{Q}|^2\right]\mathrm{d}x,\end{aligned}$$

which means the limit in (3.20) holds automatically for (2.3) and (2.12) as long as the sequence exists. Now, we only need to prove that the upper and lower limits also hold for the mixing energy.

The mixing energy (2.9) matches the form (3.11), with

$$f(x,u,p) = W(u) + |p|^2 + \omega f_a(\mathbf{Q}(x),p), \tag{3.23}$$

$\alpha(x) \equiv 0$, and $\beta(x) \equiv 1$. By substituting (3.23) in (3.14), we get

$$
\begin{aligned}
h(x,p) &= \int_0^1 \inf_{t>0} \left[\frac{W(s)}{t} + t(|p|^2 + \omega f_a(\mathbf{Q}(x),p)) \right] \mathrm{d}s \\
&= \sqrt{|p|^2 + \omega f_a(\mathbf{Q}(x),p)} \int_0^1 2\sqrt{W(s)}\,\mathrm{d}s \\
&= 2c_0 \sqrt{|p|^2 + \omega f_a(\mathbf{Q}(x),p)}.
\end{aligned} \tag{3.24}
$$

Then, using Lemma 3.2 ((3.15) and (3.16)), we immediately get the Γ-convergence of the mixing energy (2.9):

$$
\begin{aligned}
&\forall \{\phi_\varepsilon\},\ \liminf_{\varepsilon\to 0} \int_\Omega \left[\varepsilon^{-1} W(\phi) + \varepsilon \left(|\nabla\phi|^2 + \omega f_a(\mathbf{Q}, \nabla\phi) \right) \right] \mathrm{d}x \\
&\quad \geq 2c_0 \int_{\partial A} \sqrt{1 + \omega f_a(\mathbf{Q}, \boldsymbol{\nu})}\,\mathrm{d}S, \\
&\exists \{\phi_\varepsilon\},\ \text{s.t.}\ \limsup_{\varepsilon\to 0} \int_\Omega \left[\varepsilon^{-1} W(\phi) + \varepsilon \left(|\nabla\phi|^2 + \omega f_a(\mathbf{Q}, \nabla\phi) \right) \right] \mathrm{d}x \\
&\quad \leq 2c_0 \int_{\partial A} \sqrt{1 + \omega f_a(\mathbf{Q}, \boldsymbol{\nu})}\,\mathrm{d}S.
\end{aligned}
$$

Note that A in (3.13) is regarded as the region where $u = \alpha(x) = 0$, so in our case (where $\phi = 1$ on the interior of A) we should substitute A^c for A in (3.13), and $\boldsymbol{\nu}_A$ becomes $-\boldsymbol{\nu}$ on ∂A. However, the function $h(x,p)$ in our functional is symmetric in p: $h(x,p) = h(x,-p)$, so the substitution leaves the limiting functional unchanged. Also note that Lemma 3.2 is originally stated about a domain $\Omega_0 \subset \mathbb{R}^3$ with Lipschitz boundary, but our domain is the periodic space $\Omega = \mathbb{T}^3$. There is no essential difficulty in generalizing the lemma to our case since all functions in $\mathbb{T}^3$ are equivalent to periodic functions in $\mathbb{R}^3$. ∎

The limit functional in (3.17) is the combination of a bulk energy

$$
\int_A \left[\frac{1}{2\lambda} |\boldsymbol{\nabla}\mathbf{Q}|^2 + \frac{w_v \kappa}{2} |\boldsymbol{\nabla}\mathbf{Q}|^2 + \lambda \bar{F}_b(\mathbf{Q}) \right] \mathrm{d}x, \tag{3.25}
$$

a surface energy

$$
2c_0 w_p \int_{\partial A} \sqrt{1 + \omega f_a(\mathbf{Q}, \boldsymbol{\nu})}\,\mathrm{d}S, \tag{3.26}
$$

and a penalty term

$$
\frac{w_v}{2} \int_{A^c} \left[\kappa |\boldsymbol{\nabla}\mathbf{Q}|^2 + \kappa^{-1} |\mathbf{Q}|^2 \right] \mathrm{d}x. \tag{3.27}
$$

Among them, (3.25) and (3.26) correspond exactly to terms from the physical shape optimization problem (1.1), but the void term in (3.27) is still artificial. It is eliminated as $\kappa \to 0$ in another Γ-limit, as stated in Proposition 3.4.

PROPOSITION 3.4. *Suppose that $A \subset \Omega = \mathbb{T}^3$ is a C^2 region satisfying the volume constraint $|A| = V_0$. For $\mathbf{Q} \in H^1(A; \mathcal{S}_0)$, we define the sharp-interface energy*

$$
\mathscr{E}_{0,0}[\mathbf{Q}, A] = \int_A \left[\frac{1}{2\lambda} |\boldsymbol{\nabla}\mathbf{Q}|^2 + \lambda \bar{F}_b(\mathbf{Q}) \right] \mathrm{d}x + \int_{\partial A} \left[2c_0 w_p \sqrt{1 + \omega f_a(\mathbf{Q}, \boldsymbol{\nu})} + \frac{w_v}{2} |\mathbf{Q}|^2 \right] \mathrm{d}S. \tag{3.28}
$$

Then the following hold:

(a) *For all sequences* $\{\mathbf{Q}_\kappa\}$ *satisfying*

$$\mathbf{Q}_\kappa \in H_0^1(\Omega;\mathcal{S}_0), \quad \int_A (|\mathbf{Q}-\mathbf{Q}_\kappa|^2 + |\boldsymbol{\nabla}\mathbf{Q}-\boldsymbol{\nabla}\mathbf{Q}_\kappa|^2)\,\mathrm{d}x \to 0, \quad \int_{A^c} |\mathbf{Q}_\kappa|\,\mathrm{d}x \to 0 \tag{3.29}$$

as $\kappa \to 0$*, we have*

$$\liminf_{\kappa\to 0} \mathscr{E}_{0,\kappa}[\mathbf{Q}_\kappa, A] \geq \mathscr{E}_{0,0}[\mathbf{Q}, A]. \tag{3.30}$$

(b) *If* $\mathbf{Q} \in H^1(A;\mathcal{S}_0)$ *satisfies that*

$$\int_{\partial A} |\boldsymbol{\nabla}_\tau \mathbf{Q}|^2\,\mathrm{d}S < \infty, \tag{3.31}$$

where $\boldsymbol{\nabla}_\tau$ *stands for the gradient along the tangent direction, then there exists a sequence* $\{\mathbf{Q}_\kappa\}$ *satisfying* (3.29) *such that*

$$\lim_{\kappa\to 0} \mathscr{E}_{0,\kappa}[\mathbf{Q}_\kappa, A] = \mathscr{E}_{0,0}[\mathbf{Q}, A]. \tag{3.32}$$

Proof. The only term of concern is the penalty term (3.27) since (3.25) and (3.26) are continuous with respect to the limit (3.29). We also notice that the components of $\mathbf{Q}_\kappa$ are separable in (3.27), so it suffices to prove the following claims about each component Q_κ^{ij}. For notational simplicity, we abbreviate the (i,j) component of $\mathbf{Q}_\kappa$ as q_κ, and that of the limit function $\mathbf{Q}$ as q. We define

$$F_\kappa[q] = \int_{A^c} \left[\kappa|\nabla q|^2 + \kappa^{-1} q^2\right] \mathrm{d}x, \tag{3.33}$$

and we will prove that

$$\forall \{q_\kappa\} \to q,\ \liminf_{\kappa\to 0} F_\kappa[q_\kappa] \geq \int_{\partial A} q^2\,\mathrm{d}S, \tag{3.34}$$

$$\exists \{q_\kappa\} \to q,\ \text{s.t.}\ \lim_{\kappa\to 0} F_\kappa[q_\kappa] = \int_{\partial A} q^2\,\mathrm{d}S, \tag{3.35}$$

where the limit of $\{q_\kappa\}$ is taken in the sense of (3.29).

Step 1. *Lower limit* (3.34). We employ the same technique as [39, 53]. First we notice that

$$F_\kappa[q_\kappa] \geq \int_{A^c} |2q\nabla q|\,\mathrm{d}x = \int_{A^c} |\nabla(q^2)|\,\mathrm{d}x. \tag{3.36}$$

It can be equivalently written as a supremum over test functions:

$$F_\kappa[q] \geq \sup_{\substack{\mathbf{g}\in C^1(A^c)\\ |\mathbf{g}|\leq 1}} \int_{A^c} \mathbf{g}\cdot\nabla(q^2)\,\mathrm{d}x. \tag{3.37}$$

By the divergence theorem, we get

$$F_\kappa[q] \geq \sup_{\substack{\mathbf{g}\in C^1(A^c)\\ |\mathbf{g}|\leq 1}} \left[-\int_{\partial A} q^2 \mathbf{g}\cdot\boldsymbol{\nu}\,\mathrm{d}S - \int_{A^c} q^2 \nabla\cdot\mathbf{g}\,\mathrm{d}x\right], \tag{3.38}$$

where the boundary integral is evaluated on ∂A only because of our periodic boundary condition. By the elementary relation that $\liminf_{\kappa\to 0}\sup_{\mathbf{g}}[\cdots]\geq\sup_{\mathbf{g}}\liminf_{\kappa\to 0}[\cdots]$, we immediately obtain that

$$\begin{aligned}\liminf_{\kappa\to 0}F_\kappa[q_\kappa]&\geq\sup_{\substack{\mathbf{g}\in C^1(A^c)\\|\mathbf{g}|\leq 1}}\liminf_{\kappa\to 0}\left[-\int_{\partial A}q_\kappa^2\mathbf{g}\cdot\boldsymbol{\nu}\,\mathrm{d}S-\int_{A^c}q_\kappa^2\nabla\cdot\mathbf{g}\,\mathrm{d}x\right]\\&=\sup_{\substack{\mathbf{g}\in C^1(A^c)\\|\mathbf{g}|\leq 1}}\int_{\partial A}(-q^2)\mathbf{g}\cdot\boldsymbol{\nu}\,\mathrm{d}S=\int_{\partial A}q^2\,\mathrm{d}S,\end{aligned}\tag{3.39}$$

which means the lower limit in (3.34) is satisfied.

Step 2(a). *Construction of recovery sequence for upper limit* (3.35). We introduce the signed distance function (SDF) with respect to ∂A, defined as [20, 21, 14, 47, 12]

$$h(x)=\begin{cases}\operatorname{dist}(x,\partial A),\ x\notin A,\\-\operatorname{dist}(x,\partial A),\ x\in A.\end{cases}\tag{3.40}$$

The generalization of the SDF to our periodic setting $\Omega=\mathbb{T}^3$ is straightforward, as it can be defined as the SDF to the equivalent periodic region in $\mathbb{R}^3$ corresponding to A, which is also periodic. Intuitively, $h(x)$ depicts locally the "altitude" above or below the surface ∂A. Some important property of $h(x)$ includes that it has the same smoothness as ∂A, and that it satisfies $|\nabla h|=1$ almost everywhere. For each $\kappa>0$, we define the extension

$$q_\kappa(x)=\begin{cases}q(x), & x\in A,\\ q(x^\perp)\exp(-h(x)/\kappa), & 0\leq h(x)<\sqrt{\kappa},\\ q(x^\perp)\mathrm{e}^{-\kappa^{-\frac{1}{2}}}\dfrac{2\sqrt{\kappa}-h(x)}{\sqrt{\kappa}}, & \sqrt{\kappa}\leq h(x)<2\sqrt{\kappa},\\ 0, & h(x)\geq 2\sqrt{\kappa},\end{cases}\tag{3.41}$$

where $x^\perp$ is the orthogonal projection of x on ∂A satisfying $|h(x)|=|x-x^\perp|$. The extension (3.41) works by shrinking the initial value $q(x^\perp)$ exponentially along the normal direction for a distance of $\sqrt{\varepsilon}$, then cutting it down to 0 at the distance $2\sqrt{\varepsilon}$, and finally interpolating linearly in between. See Figure 3.1 for an illustration of q_κ in the normal direction. The fact that $q_\kappa\in H^1(\Omega)$ will be demonstrated later.

In order to characterize q_κ, we need to digress and discuss the projection $x\mapsto x^\perp$. Obviously, it satisfies

$$y=x^\perp\Leftrightarrow x=y+t\boldsymbol{\nu}(y)\tag{3.42}$$

for all $y\in\partial A$ and x sufficiently close to ∂A. Moreover, $\nabla h(x)$ is constantly equal to the unit normal vector $\boldsymbol{\nu}(x^\perp)$ along the normal direction stemming from $x^\perp$, which

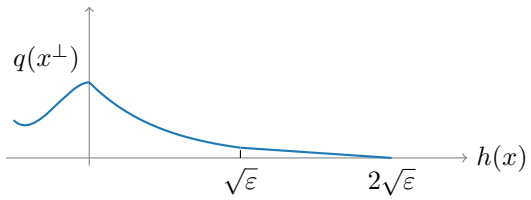

FIG. 3.1. *Illustration for the extension* (3.41) *along the normal direction.*

indicates that $h(x) \equiv \boldsymbol{\nu}(y)$ for all x in (3.42); the definition of $x^\perp$ also indicates that $|x-y| = |h(x)|$. Therefore, for all $x \in A^c$ close enough to ∂A, we have

$$x^\perp = x - h(x)\nabla h(x) = x - \frac{1}{2}\nabla(h^2). \tag{3.43}$$

Since A is C^2 by assumption, $h(x)$ is also C^2, so the mapping $x \mapsto x^\perp$ given by (3.43) above is C^1, and its Jacobian matrix equals

$$\mathbf{J}(x) = \nabla_x x^\perp = \mathbf{I} - \frac{1}{2}\nabla^2(h^2), \tag{3.44}$$

which is symmetric and continuous in a neighborhood of ∂A.

Define

$$\iota_\kappa(h) = \begin{cases} \exp(-h/\kappa), & 0 \le h < \sqrt{\kappa}, \\ \mathrm{e}^{-\kappa^{-\frac{1}{2}}} \dfrac{2\sqrt{\kappa} - h}{\sqrt{\kappa}}, & \sqrt{\kappa} \le h < 2\sqrt{\kappa}, \\ 0, & h \ge 2\sqrt{\kappa}, \end{cases} \tag{3.45}$$

which is a Lipschitz continuous function. $q_\kappa(x)$ can be written more compactly as $q(x^\perp)\iota_\kappa(h(x))$ when $x \notin A$. By the chain rule,

$$\nabla q_\kappa(x) = \mathbf{J}(x)\nabla q(x^\perp) + q(x^\perp)\iota_\kappa'(h(x))\nabla h(x), \ x \notin A, \tag{3.46}$$

provided κ is sufficiently small so that the support of q_κ falls inside the neighborhood where the expressions for $x^\perp$ (3.43) and $\mathbf{J}(x)$ (3.44) are valid. Since the image of the mapping $x \mapsto x^\perp$ stays in ∂A, the columns of its Jacobian matrix $\mathbf{J}(x)$ from (3.44) are perpendicular to the normal vector $\boldsymbol{\nu}(x^\perp) = \nabla h(x)$. By the symmetry of $\mathbf{J}(x)$, the rows of $\mathbf{J}(x)$ are also perpendicular to $\boldsymbol{\nu}$, so the first term of (3.46) can be written alternatively as $\mathbf{J}(x)\nabla_\tau q(x^\perp)$ (∇_τ is the directional gradient along the tangent direction), i.e.,

$$\nabla q_\kappa(x) = \mathbf{J}(x)\nabla_\tau q(x^\perp) + q(x^\perp)\iota_\kappa'(h(x))\nabla h(x). \tag{3.47}$$

Note that (3.47) is formally an orthogonal decomposition of ∇q_κ along the tangent and normal directions. By the Pythagorean theorem,

$$|\nabla q_\kappa|^2 = |\mathbf{J}(x)\nabla_\tau q(x^\perp)|^2 + |q(x^\perp)|^2|\iota_\kappa'(h(x))|^2. \tag{3.48}$$

Equation (3.47) also shows that q_κ belongs to $H^1(\Omega)$ because q_κ is continuous in the normal direction by its definition (3.41) and that (3.47) presents its explicit weak derivative. The integral of $|\nabla q_\kappa|^2$ will be shown to be finite in the following computation.

Step 2(b). *Computation of upper limit* (3.35). We explicitly compute $F_\kappa[q_\kappa]$ using the coarea formula [21, 11, 12]

$$F_\kappa[q_\kappa] = \int_0^{2\sqrt{\kappa}} \mathrm{d}r \int_{\{h=r\}} (\kappa|\nabla q_\kappa|^2 + \kappa^{-1}q_\kappa^2)\,\mathrm{d}S \triangleq \int_0^{2\sqrt{\kappa}} I_r\,\mathrm{d}r, \tag{3.49}$$

where $\{h = r\}$ denotes the r-level set of $h(x)$. The factor $|\nabla h|$ has been ignored since $|\nabla h| = 1$ a.e. Next, we compute the surface integral I_r. The level set $\{h = r\}$ can be parametrized with $y \in \partial A$ by the formula

$$\{h = r\} = \{y + r\boldsymbol{\nu}(y) : y \in \partial A\}, \tag{3.50}$$

which is continuously differentiable given $\partial A \in C^2$. Hence, by using the expressions in (3.41) and (3.48), we get

(3.51)
$$\begin{aligned} I_r &= \int_{\{h=r\}} \left[\kappa|\mathbf{J}(x)\nabla_\tau q(x^\perp)|^2 + \kappa|q(x^\perp)|^2|\iota_\kappa'(h(x))|^2 + \kappa^{-1}|q(x^\perp)|^2|\iota_\kappa(h(x))|^2\right] \mathrm{d}S(x) \\ &= \int_{\partial A} \left[\kappa|\mathbf{J}(y+r\boldsymbol{\nu})\nabla_\tau q(y)|^2 + \kappa|q(y)|^2|\iota_\kappa'(r)|^2 + \kappa^{-1}|q(y)|^2|\iota_\kappa(r)|^2\right] \gamma(y,r)\,\mathrm{d}S(y), \end{aligned}$$

where $\gamma(y,r)$ is the scaling factor of area elements that satisfies $\gamma(y,r) \to 1$ uniformly in $y \in \partial A$ as $r \to 0$. By the assumption (3.31) and the continuity of $\mathbf{J}$, the first term of I_r is controlled by

$$\int_{\partial A} \kappa|\mathbf{J}(y+r\boldsymbol{\nu})\nabla_\tau q(y)|^2\gamma(y,r)\,\mathrm{d}S(y) \le C(\mathbf{J})\kappa \int_{\partial A} |\nabla_\tau q|^2\,\mathrm{d}S \to 0 \tag{3.52}$$

as $\kappa \to 0$. Since I_r is integrated over the interval $r \in [0, 2\sqrt{\kappa}]$ which also shrinks to 0, the first term can be ignored. Hence, we only need to evaluate the remaining terms, which can be reorganized into

$$\tilde{I}_r = (\kappa|\iota_\kappa'(r)|^2 + \kappa^{-1}|\iota_\kappa(r)|^2) \int_{\partial A} |q(y)|^2\gamma(y,r)\,\mathrm{d}S(y). \tag{3.53}$$

It is then straightforward to compute from (3.45) that

(3.54)
$$\begin{aligned} &\lim_{\kappa\to 0} \int_0^{2\sqrt{\kappa}} I_r\,\mathrm{d}r = \lim_{\kappa\to 0} \int_0^{2\sqrt{\kappa}} \tilde{I}_r\,\mathrm{d}r \\ &= \lim_{\kappa\to 0} \int_{\partial A} |q|^2\,\mathrm{d}S(y) \left[\int_0^{\kappa^{\frac{1}{2}}} \gamma(y,r)\cdot\frac{2}{\kappa}\mathrm{e}^{-2r/\kappa}\,\mathrm{d}r + \int_{\kappa^{\frac{1}{2}}}^{2\kappa^{\frac{1}{2}}} \gamma(y,r)\cdot O(\kappa^{-1}\mathrm{e}^{-2\kappa^{-\frac{1}{2}}})\,\mathrm{d}r\right]. \end{aligned}$$

As $\kappa^{-1}\mathrm{e}^{-2\kappa^{-\frac{1}{2}}} \to 0$, we have

$$\begin{aligned} \lim_{\kappa\to 0} F_\kappa[q_\kappa] &= \lim_{\kappa\to 0} \int_0^{2\sqrt{\kappa}} I_r\,\mathrm{d}r \\ &= \lim_{\kappa\to 0} \int_{\partial A} |q|^2\,\mathrm{d}S(y) \int_0^{\kappa^{\frac{1}{2}}} \gamma(y,r)\cdot\frac{2}{\kappa}\mathrm{e}^{-2r/\kappa}\,\mathrm{d}r \\ &= \lim_{\kappa\to 0} \int_{\partial A} |q|^2\,\mathrm{d}S(y) \int_0^{\kappa^{-\frac{1}{2}}} \gamma(y,\kappa t)\cdot 2\mathrm{e}^{-2t}\,\mathrm{d}t = \int_{\partial A} |q|^2\,\mathrm{d}S, \end{aligned} \tag{3.55}$$

which means the upper limit in (3.35) is satisfied. ∎

Proposition 3.4 eliminates the penalty term on the exterior of A and results in a sharp-interface free-boundary energy functional (3.28) defined for region A and tensor-valued function $\mathbf{Q}$ that matches the form (1.1), with bulk energy density

$$W(\mathbf{Q}, \boldsymbol{\nabla}\mathbf{Q}) = \frac{1}{2\lambda}|\boldsymbol{\nabla}\mathbf{Q}|^2 + \lambda\bar{F}_b(\mathbf{Q}) \tag{3.56}$$

and surface density

$$F_a(\mathbf{Q}, \boldsymbol{\nu}) = 2c_0 w_p\sqrt{1+\omega f_a(\mathbf{Q},\boldsymbol{\nu})} + \frac{w_v}{2}|\mathbf{Q}|^2. \tag{3.57}$$

If w_v is small, the artificial $|\mathbf{Q}|^2$ penalty term in F_a can be ignored, so what is left in (3.57) is a physically relevant boundary anchoring energy. Therefore, our diffuse-interface model in (2.1) is not only computationally efficient but also a good approximation of the sharp-interface energy of NLC droplets in (1.1).

4. Asymptotic solutions. The diffuse-interface model (2.1) is governed by the LdG free energy in the region $\phi = 1$ (interior of the droplet), while the void penalty imposes the constraint $\mathbf{Q} \equiv 0$ in the region $\phi = 0$ (exterior of the droplet). What remains unclear is the behavior of the model within the diffuse interface $0 < \phi < 1$. In this section, we provide more insight into the diffuse-interface behavior by constructing a heuristic asymptotic solution $(\phi, \mathbf{Q})$ as $\varepsilon, \kappa \to 0$.

We simplify the problem by considering 1D functions $\mathbf{Q} = \mathbf{Q}(z), \phi = \phi(z)$, with $\mathbf{Q}(z) = s(z)(\mathbf{n} \otimes \mathbf{n} - \frac{1}{3}\mathbf{I})$ being uniaxial everywhere, and the director $\mathbf{n} \in \mathbb{S}^2$ being constant. In other words, we study the phase transition along the normal direction of the xOy surface. We also assign simple values to model constants λ, w_p, w_v in order to emphasize the effect of small parameters ε, κ. Then, the energy functional (2.1) is reduced to

$$\begin{aligned}\tilde{E}[s,\phi] = &\int_{\mathbb{R}} \phi^2 \left[H(s) + \frac{1}{2}|s'|^2 \right] \mathrm{d}z \\ &+ \frac{1}{2}\int_{\mathbb{R}} \left[\varepsilon^{-1} W(\phi) + \varepsilon |\phi'|^2 \left(1 + \omega \left| s(\mathbf{n}\cdot\mathbf{e}_z)\mathbf{n} + \frac{s_+ - s}{3}\mathbf{e}_z \right|^2 \right) \right] \mathrm{d}z \\ &+ \frac{1}{2}\int_{\mathbb{R}} \left[\kappa |s'|^2 + \kappa^{-1}(1-\phi)^2 s^2 \right] \mathrm{d}z,\end{aligned} \tag{4.1}$$

where $H(s) = \frac{3A}{4C}s^2 - \frac{B}{6C}s^3 + \frac{1}{4}s^4$ is the LdG bulk energy (2.6) expressed in terms of s, $\mathbf{e}_z$ is the unit vector oriented in the z direction, and $\lambda = 1, w_p = \frac{1}{2}, w_v = 1$. To describe a phase transition from the nematic droplet to isotropic phase, we impose boundary conditions on ϕ:

$$\phi(-\infty) = 1, \ \phi(+\infty) = 0. \tag{4.2}$$

Since the sharp-interface limit with respect to ε (Proposition 3.3) occurs before the one with respect to κ (Proposition 3.4), we make ε significantly smaller than κ to emulate such a paradigm. For technical purposes, we assume that

$$\varepsilon = o(\kappa^2) \tag{4.3}$$

as $\kappa \to 0$.

We consider the tangential boundary anchoring, i.e., $\mathbf{n} \perp \mathbf{e}_z$, so that (4.1) becomes

$$\begin{aligned}\tilde{E}[s,\phi] = &\int_{\mathbb{R}} \phi^2 \left[H(s) + \frac{1}{2}|s'|^2 \right] \mathrm{d}z + \frac{1}{2}\int_{\mathbb{R}} \left[\varepsilon^{-1} W(\phi) + \varepsilon |\phi'|^2 \left(1 + \frac{\omega}{9}(s - s_+)^2 \right) \right] \mathrm{d}z \\ &+ \frac{1}{2}\int_{\mathbb{R}} \left[\kappa |s'|^2 + \kappa^{-1}(1-\phi)^2 s^2 \right] \mathrm{d}z.\end{aligned} \tag{4.4}$$

The Euler–Lagrange equation of (4.4) is

$$(\phi^2 s')' + \kappa s'' = \phi^2 H'(s) + \kappa^{-1}(1-\phi)^2 s + \frac{\omega\varepsilon|\phi'|^2}{9}(s - s_+), \tag{4.5}$$

$$\varepsilon \left(\left(1 + \frac{\omega}{9}(s - s_+)^2 \right) \phi' \right)' = \frac{1}{2}\varepsilon^{-1} W'(\phi) + \kappa^{-1} s^2 (\phi - 1) + 2\left(H(s) + \frac{1}{2}|s'|^2 \right)\phi. \tag{4.6}$$

We make the following ansatz:

$$\phi(z) = \Phi\left(\frac{z}{\varepsilon}\right), \ s(z) = S\left(\frac{z}{\kappa}\right). \tag{4.7}$$

Then, (4.5) and (4.6) become

(4.8)
$$\frac{2}{\varepsilon\kappa}\Phi\left(\frac{z}{\varepsilon}\right)\Phi'\left(\frac{z}{\varepsilon}\right)S'\left(\frac{z}{\kappa}\right)+\frac{1}{\kappa^2}\Phi^2\left(\frac{z}{\varepsilon}\right)S''\left(\frac{z}{\kappa}\right)+\frac{1}{\kappa}S''\left(\frac{z}{\kappa}\right)$$
$$=\Phi^2\left(\frac{z}{\varepsilon}\right)H'\left(S\left(\frac{z}{\kappa}\right)\right)+\frac{1}{\kappa}\left(1-\Phi\left(\frac{z}{\varepsilon}\right)\right)^2S\left(\frac{z}{\kappa}\right)+\frac{\omega}{9\varepsilon}\left(\Phi'\left(\frac{z}{\varepsilon}\right)\right)^2\left(S\left(\frac{z}{\kappa}\right)-s_+\right),$$

(4.9)
$$\frac{1}{\varepsilon}\left[1+\frac{\omega}{9}\left(S\left(\frac{z}{\kappa}\right)-s_+\right)^2\right]\Phi''\left(\frac{z}{\varepsilon}\right)+\frac{2\omega}{9\kappa}\left(S\left(\frac{z}{\kappa}\right)-s_+\right)S'\left(\frac{z}{\kappa}\right)\Phi'\left(\frac{z}{\varepsilon}\right)$$
$$=\frac{1}{2\varepsilon}W'\left(\Phi\left(\frac{z}{\varepsilon}\right)\right)+\frac{1}{\kappa}S^2\left(\frac{z}{\kappa}\right)\left(\Phi\left(\frac{z}{\varepsilon}\right)-1\right)+2\left[H\left(S\left(\frac{z}{\kappa}\right)\right)+\frac{1}{2\kappa^2}S'\left(\frac{z}{\kappa}\right)\right]\Phi\left(\frac{z}{\varepsilon}\right).$$

We first reorganize (4.9) as

(4.10)
$$\frac{1}{\varepsilon}\left[\left(1+\frac{\omega}{9}(S(rt)-s_+)^2\right)\Phi''(t)-\frac{1}{2}W'(\Phi(t))\right]-\frac{1}{\kappa^2}S'(rt)\Phi(t)$$
$$+\frac{1}{\kappa}\left[\frac{2\omega}{9}(S(rt)-s_+)S'(rt)\Phi'(t)-\frac{1}{\kappa}S^2(rt)(\Phi(t)-1)\right]-2H(S(rt))\Phi(t)=0,$$

where $t=z/\varepsilon$ and $r=\varepsilon/\kappa$. Since we assumed $\varepsilon\ll\kappa^2$ in (4.3), the leading terms of (4.10) are the $O(\varepsilon^{-1})$ terms. Hence, (4.10) is asymptotically dominated by

$$\tilde{\Phi}''(t)=\frac{1}{1+\frac{\omega}{9}(S(0)-s_+)^2}\cdot\frac{1}{2}W'(\tilde{\Phi}(t)). \tag{4.11}$$

Notice that we have replaced $S(rt)$ with $S(0)$ because $r=\varepsilon\kappa\to 0$ by (4.3). With $W(s)=s^2(1-s)^2$, (4.11) allows an analytic standing-wave solution [13]

$$\tilde{\Phi}(t)=\frac{1}{2}-\frac{1}{2}\tanh\frac{t}{2\sqrt{1+\frac{\omega}{9}(S(0)-s_+)^2}}, \tag{4.12}$$

satisfying the boundary condition (4.2), which indicates that the phase field $\phi(z)=\Phi(\frac{z}{\varepsilon})$ changes from 1 to 0 within a layer of thickness $O(\varepsilon)$.

We substitute (4.12) for Φ in (4.8) and get

(4.13)
$$\frac{1}{\kappa^2}\tilde{\Phi}^2\left(\frac{\tau}{r}\right)S''(\tau)+\frac{1}{\kappa}\left[S''(\tau)-\underline{\left(1-\tilde{\Phi}\left(\frac{\tau}{r}\right)\right)^2S(\tau)}\right]$$
$$+\frac{1}{\kappa^2}\underline{\frac{2}{r}\tilde{\Phi}\left(\frac{\tau}{r}\right)}\tilde{\Phi}'\left(\frac{\tau}{r}\right)S'(\tau)-\underline{\frac{1}{\kappa}\frac{\omega}{9r}\left(\tilde{\Phi}'\left(\frac{\tau}{r}\right)\right)^2}(S(\tau)-s_+)-\tilde{\Phi}^2\left(\frac{\tau}{r}\right)H'(S(\tau))=0,$$

where $\tau=z/\kappa$ and $r=\varepsilon/\kappa\to 0$. For any fixed $\tau<0$, as $r\to 0$, $\tilde{\Phi}(\tau/r)$ approaches 1 and $\tilde{\Phi}'(\tau/r)$ approaches 0 exponentially, according to (4.12). Therefore, the following terms in (4.13), as marked by underlines, are infinitesimal compared to any polynomial order k:

$$\left(1-\tilde{\Phi}\left(\frac{\tau}{r}\right)\right)^2=o(r^k),\quad \frac{2}{r}\tilde{\Phi}\left(\frac{\tau}{r}\right)\tilde{\Phi}'\left(\frac{\tau}{r}\right)=o(r^k),\quad \frac{1}{r}\left(\tilde{\Phi}'\left(\frac{\tau}{r}\right)\right)^2=o(r^k). \tag{4.14}$$

Thus, the leading term of (4.13) is the $O(\kappa^{-2})$ term, and we get the dominating equation

$$S''(\tau)=O(\kappa^2). \tag{4.15a}$$

Note that the $O(\kappa^{-1})$ term is absorbed by the leading order since they are both equal to $S''(\tau)$. For any fixed $\tau > 0$, we have that $\tilde{\Phi}(\tau/r) \to 0$ and $\tilde{\Phi}'(\tau/r) \to 0$ exponentially. Thus, for $\tau > 0$, the first term of (4.13) becomes infinitesimal compared to any polynomial order k:

$$\frac{1}{\kappa^2}\tilde{\Phi}^2\left(\frac{\tau}{r}\right) = o(\kappa^k) \tag{4.15b}$$

because $r = o(\kappa)$ by the assumption (4.3). Hence, for $\tau > 0$, the leading orders of (4.13) are the $O(\kappa^{-1})$ terms:

$$S''(\tau) = S(\tau) + O(\kappa). \tag{4.15c}$$

Then, we get the following bounded asymptotic solution to (4.15):

$$\tilde{S}(\tau) = \begin{cases} X_0, & \tau < 0, \\ X_0 \mathrm{e}^{-\tau}, & \tau > 0, \end{cases} \tag{4.16}$$

which indicates that the scalar order parameter $s(z)$ decreases exponentially to 0 within a region of thickness κ on the exterior of the droplet (where $\phi = 0$).

To further compute X_0, we study the behavior of $\tilde{S}(\tau)$ near $\tau = 0$. Integrating (4.13) over an interval $[-h, h]$, we get

$$\begin{aligned} &\frac{1}{\kappa}\left[\tilde{\Phi}^2\left(\frac{h}{r}\right)S'(h) - \tilde{\Phi}^2\left(-\frac{h}{r}\right)S'(-h)\right] + [S'(h) - S'(-h)] \\ &\quad = \int_{-h}^{h}\left(1 - \tilde{\Phi}\left(\frac{\tau}{r}\right)\right)^2 S(\tau)\,\mathrm{d}\tau + \frac{\omega}{9}\int_{-h}^{h}\frac{1}{r}\left(\tilde{\Phi}'\left(\frac{\tau}{r}\right)\right)^2 (S(\tau) - s_+)\,\mathrm{d}\tau + O(\kappa) \\ &\quad = \frac{\omega}{9}\int_{-h/r}^{h/r}(\tilde{\Phi}'(u))^2 (S(ru) - s_+)\,\mathrm{d}u + O(\kappa + h). \end{aligned} \tag{4.17}$$

For any fixed h, $\tilde{\Phi}(h/r)$ approaches 0 exponentially as $r \to 0$ so

$$\frac{1}{\kappa}\tilde{\Phi}^2\left(\frac{h}{r}\right)S'(h) = o(\kappa), \tag{4.18}$$

and $S'(-h) = O(\kappa^2)$ by (4.15a), so

$$\frac{1}{\kappa}\tilde{\Phi}^2\left(-\frac{h}{r}\right)S'(-h) = o(1). \tag{4.19}$$

Thus, for any fixed h, as $\kappa, r \to 0$, the first bracket on the left-hand side of (4.17) becomes

$$\frac{1}{\kappa}\left[\tilde{\Phi}^2\left(\frac{h}{r}\right)S'(h) - \tilde{\Phi}^2\left(-\frac{h}{r}\right)S'(-h)\right] \to 0, \tag{4.20}$$

and the second bracket therein becomes

$$S'(h) - S'(-h) \to -X_0 \mathrm{e}^{-h} \tag{4.21}$$

by (4.16). The integral on the right-hand side of (4.17) becomes

$$\int_{-\infty}^{\infty}(\tilde{\Phi}'(u))^2 (S(0) - s_+)\,\mathrm{d}u = (X_0 - s_+)\int_{-\infty}^{\infty}(\tilde{\Phi}'(u))^2\,\mathrm{d}u = \frac{X_0 - s_+}{6\sqrt{1 + \frac{\omega}{9}(X_0 - s_+)^2}}, \tag{4.22}$$

as is computed from (4.12). Hence, under the asymptotic limit $r, \kappa \to 0$, (4.17) becomes

$$-X_0 \mathrm{e}^{-h} = \frac{\omega}{9} \frac{X_0 - s_+}{6\sqrt{1 + \frac{\omega}{9}(X_0 - s_+)^2}} + O(h). \tag{4.23}$$

Therefore, letting $h \to 0$ shows that $x = X_0$ is a solution to the equation

$$x + \frac{\frac{\omega}{9}(x - s_+)}{6\sqrt{1 + \frac{\omega}{9}(x - s_+)^2}} = 0. \tag{4.24}$$

We observe that since the left-hand side of (4.24) is strictly increasing in x and blows up to infinity as $x \to \pm\infty$, (4.24) admits a unique solution $X_0 \in \mathbb{R}$, which depends solely on s_+ and ω.

In summary, (4.12), (4.16), and (4.24) together characterize the asymptotic behavior of the interface between the NLC droplet and the exterior isotropic liquid. The profiles of the asymptotic solutions $\phi(z)$ and $s(z)$ are shown in Figure 4.1(a), which illustrates the fact that the interface width of the orientational order (κ) is larger than that of the phase field order parameter (ε). The value of X_0 is determined uniquely by the relation (4.24) as a function of ω, which is plotted in Figure 4.1(b) using the parameters (5.1). It shows that X_0 approximates s_+ indefinitely as ω

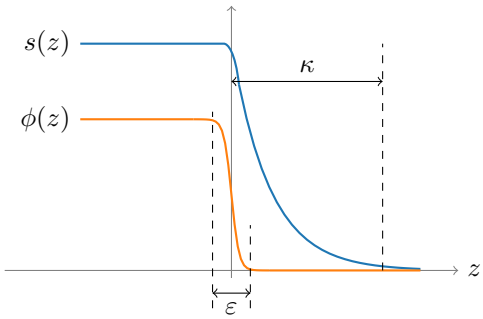

(a)

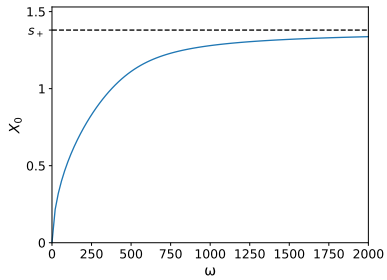

(b)

FIG. 4.1. *Solution profiles of the asymptotic solutions and the constant* X_0. (a) *Solution profiles of* $s(z)$ *and* $\phi(z)$ *according to the ansatz* (4.7) *and the expressions* (4.16) *and* (4.12). s *changes within an interval of size* $O(\kappa)$, *while* ϕ *changes within an interval of* $O(\varepsilon)$. (b) *Relation of* X_0 *and* ω *according to* (4.24), *with* $s_+ \approx 1.38$ *marked by a black dashed line.*

grows larger, which means that strong boundary anchoring forces the boundary tensor $\mathbf{Q}(0) = s(0)(\mathbf{n} \otimes \mathbf{n} - \frac{1}{3}\mathbf{I})$ to satisfy the planar anchoring condition with $s(0) = s_+$.

5. Numerical results. In this section, we numerically study equilibrium configurations of (2.1). We take model parameters to be

$$a = -\frac{866}{3500},\ b = \frac{6400}{3500},\ V_0 = 0.1,\ \varepsilon = 0.005,\ \omega = 20,\ w_p = 1,\ w_v = 0.5, \tag{5.1}$$

and $\kappa = \sqrt{\varepsilon}$. Although the asymptotic analysis in section 4 requires that $\varepsilon = o(\kappa^2)$, our numerical tests show that this setting is sufficient to produce sharp boundaries for both $\mathbf{Q}$ and ϕ. The constants a, b roughly correspond to the commonly used NLC material N-(p-methoxybenzylidene)-p-butylaniline at a lower temperature [35, 24, 50]. The nondimensional domain size λ is related to the physical scale l_0 (unit m) by $\lambda^2 = l_0^2 C/L$ with $C = 3500\,\mathrm{N}\ \cdot\ \mathrm{m}^{-2}, L = 4 \times 10^{-11}\,\mathrm{N}$ being physical constants.

5.1. Numerical methods. We use a finite difference method to discretize $\Omega = \mathbb{T}^3$, or equivalently the unit cube $[0,1]^3$ with periodic boundary conditions. The order parameters $\mathbf{Q}, \phi$ from the admissible space (3.1) are evaluated at an $N \times N \times N$ periodic grid $(x_{j_1}, y_{j_2}, z_{j_3}) = (j_1 h, j_2 h, j_3 h)$ with $h = N^{-1}$ and all indices having period N. The traceless tensor $\mathbf{Q}$ has 5 independent degrees of freedom, so we parametrize it with 5 scalar functions q_1–q_5:

$$\mathbf{Q} = \begin{bmatrix} q_1 - q_3 & q_2 & q_4 \\ q_2 & -q_1 - q_3 & q_5 \\ q_4 & q_5 & 2q_3 \end{bmatrix}. \tag{5.2}$$

The grid functions q_i are denoted by $\{q^{(i)}_{j_1 j_2 j_3}\}$ $(i = 1, \ldots, 5)$. ϕ is defined on a staggered grid offset by $h/2$ in each dimension, denoted by $\{\phi_{j_1+\frac{1}{2}, j_2+\frac{1}{2}, j_3+\frac{1}{2}}\}$.

We then use a finite difference method to evaluate the energy (2.1). Functions are numerically integrated by summing over the grid sites

$$\int_\Omega F(x)\,\mathrm{d}x \approx h^3 \sum_{j_1, j_2, j_3 = 0}^{N-1} F(x_{j_1}, y_{j_2}, z_{j_3}), \tag{5.3}$$

and derivatives are evaluated using the central difference, so that there is second-order accuracy. The volume constraint (2.2) is discretized as

$$h^3 \sum_{j_1, j_2, j_3 = 0}^{N-1} \phi_{j_1+\frac{1}{2}, j_2+\frac{1}{2}, j_3+\frac{1}{2}} = V_0. \tag{5.4}$$

The numerical evaluation of (2.1) yields a finite-dimensional function $\mathscr{E}^h$ of $\{q^{(i)}_{j_1 j_2 j_3}\}$ $(i = 1, \ldots, 5)$ and $\{\phi_{j_1+\frac{1}{2}, j_2+\frac{1}{2}, j_3+\frac{1}{2}}\}$. We explicitly compute its gradient, whose ϕ component is projected to the tangent space of the constraint (5.4) by subtracting its mean. Thus, any gradient descent algorithm using the projected gradient automatically preserves the volume constraint. We solve for critical points with the conjugate gradient algorithm of SciPy. After obtaining the critical point, we also explicitly compute the Hessian of the projected gradient, which is itself a symmetric operator restricted to the tangent space of (5.4). We use LOBPCG [30] to solve for its smallest eigenvalues. If the smallest eigenvalue is nonnegative, then we consider the configuration stable.

5.2. Stable configurations. In the rest of this section, we use $N = 64$. We use $\mathbf{Q} \equiv 0$ for an initial guess of the gradient descent algorithm. As for ϕ, we set it as a mollified indicator function of a predetermined droplet shape.

In Figure 5.1, we present three types of coexisting (meta)stable configurations under the parameters (5.1) and different values of λ, all of which appear rotationally symmetric to the z axis. Configurations in the first row of Figure 5.1 are radially symmetric. To obtain these configurations, the initial values of ϕ are spherically symmetric. The droplet is a perfect sphere filled with biaxial states (illustrated as flat discs) whose preferred directions are tangent to the spherical shells radiating from the center, at which there is a point defect. As a result, the planar anchoring condition on the interface is satisfied. Configurations in the second row of Figure 5.1 are called "rings." Their initial values of ϕ are oblate spheroids with short axes in the z direction, and so are the resulting droplet shapes. The ring configurations are also filled with biaxial states. They also have circular line defects (or disclination rings) perpendicular to the z axis in their centers. The value of the biaxiality field around the line defect is consistent with [31]. Configurations in the final row of Figure 5.1 are the tactoids. Their initial values for ϕ are prolate spheroids with long axes in the z direction, and so are the resulting droplet shapes. The tactoids are mostly filled with uniaxial tensors (illustrated as small rods), with a pair of point defects located symmetrically on the longer axis. As λ increases, the radial and ring configurations lose stability, while tactoids become the global minimizer. The disclination ring in the ring configuration grows in radius and moves closer to the boundary, and the droplet shape becomes more oblate as it expands in the xy plane and shrinks in the z direction. The uniaxial region of the tactoid configuration expands and pushes the defects toward the interface, while the droplet shape becomes more prolate as it shrinks in the xy plane and expands in the z direction. At $\lambda = 100$, the tactoid configuration becomes spindle-shaped, which is shown in the lower-right corner of Figure 5.1.

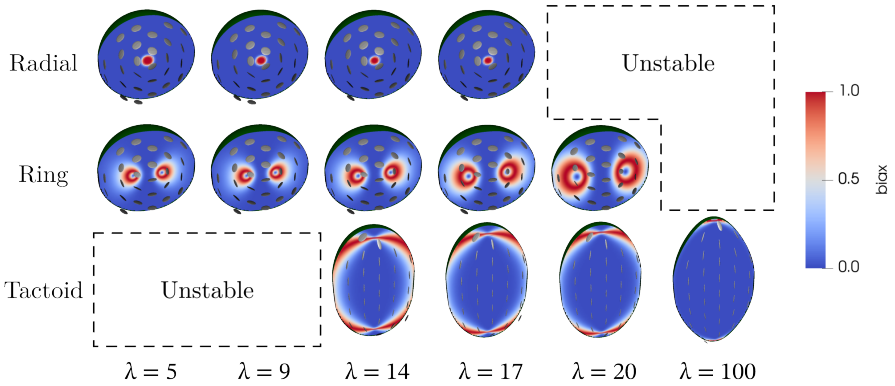

FIG. 5.1. *Three coexisting (meta)stable configurations, with parameters* (5.1) *and* $\lambda = 5, 9, 14, 17, 20, 100$, *respectively. Droplet boundary (green) is the level set* $\phi = 0.5$. *Color indicates biaxiality* $\beta = 1 - 6 \cdot \frac{(\mathrm{tr}\,\mathbf{Q}^3)^2}{(\mathrm{tr}\,\mathbf{Q}^2)^3}$, *which measures the deviation of* $\mathbf{Q}$ *from a uniaxial tensor. Director distribution is visualized via ellipsoids, whose principal axes are parallel to eigenvectors of* $\mathbf{Q}$, *and whose axes' lengths are ordered correspondingly to eigenvalues of* $\mathbf{Q}$. *For example, in the tactoid the tensor* $\mathbf{Q}$ *has one positive and two negative eigenvalues, so the ellipsoid is significantly longer in one of its axes, and is hence reduced to a rod. (Color figure available online.)*

The disclination ring identical to our ring configuration has been derived theoretically and computationally for NLC confined in a fixed ball [38, 25]. Our simulations show that the optimal droplet shape for the disclination ring is not a symmetric ball, but rather an oblate spheroid due to interactions between defects and the droplet boundary. The spindle-shaped tactoid has been observed in numerous experiments [26, 28, 54]. It has also been predicted theoretically [19, 27]. Our simulation results, especially those in large domains, correctly reproduce the expected droplet shape.

The stable configurations in Figure 5.1 demonstrate the underlying interactions between the NLC state (represented by $\mathbf{Q}$) and the shape of the droplet (represented by ϕ). First, the defect structure influences the droplet shape, which can be observed from the ring and tactoid configurations at different scales—their optimal shapes are respectively oblate and prolate spheres instead of symmetric spheres. A possible explanation for this phenomenon is that the boundary anchoring term (2.10) forbids defects from appearing at the boundary, so that the optimal shape tends to maintain a fixed distance between the boundary and the defects. Consequently, the disclination ring in the ring configuration forces the droplet to expand in the equator on the xy plane, so it shrinks in the direction of the poles as a result of volume preservation and results in an oblate spheroid. In contrast, point defects in the tactoid configuration push the poles of the droplet away from the center, so the equator shrinks in return, rendering the overall shape prolate. In addition, the droplet shape also influences the interior nematic directors. It can be seen from the tactoid configurations in Figure 5.1 that with a more prolate spheroidal droplet, the pair of $+1/2$ nematic defects are farther away from each other and closer to the poles on the z axis. For larger λ, defects are energetically unfavorable, so the optimal droplet shape evolves pointy ends to push the defects out of the boundary and make the interior $\mathbf{Q}$-tensors fully uniaxial. The ultimate result of this transformation is the tactoid.

We show in Figure 5.2 the phase transition phenomenon of global minimizers of E_ε as λ increases at different temperature a. It can be directly observed that this phase transition of minimizers from radial and ring configurations (which are very close to each other in energy) to the tactoid is of first order, since the energy curves of the ring and radial configurations and of the tactoid intersect with different slopes. The radial, ring, and tactoid configurations coexist as stable states in a range of λ, but the radial and ring configurations lose stability as λ increases, with radial destabilizing before ring, as observed in Figure 5.2(a). The complete phase diagram with respect to domain

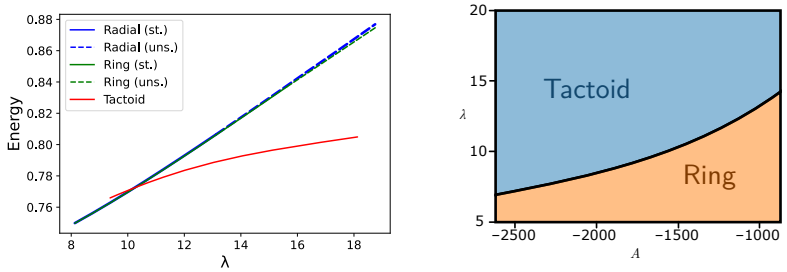

(a) (b)

FIG. 5.2. *Phase transition with respect to λ and unscaled temperature $A = a \cdot C$.* (a) *Energy values of the radial (blue), ring (green), and tactoid (red) configurations are plotted against λ at temperature $A = -1300\,\mathrm{N} \cdot \mathrm{m}^{-2}$. Dashed lines indicate unstable states.* (b) *Phase diagram of $\mathscr{E}_{\varepsilon,\kappa}$ with respect to A and λ. The parameter domains of different stable states are distinguished by different colors. The range of $A/(\mathrm{N} \cdot \mathrm{m}^{-2})$ is $(-2600, -866)$, and the range of λ is $(5, 20)$. (Color figure available online.)*

size λ and temperature a is computed laboriously and presented in Figure 5.2(b) (all parameters except λ, A are fixed as in (5.1)). According to the phase diagram, the ring configuration is generally stable at smaller λ and higher a, and the tactoid is stable at larger λ and lower a. The global minimizer of the energy functional shifts from the biaxial ring configuration to the uniaxial tactoid configuration as λ increases and/or a decreases.

The phase diagram with respect to λ and a can be explained by observing the sharp-interface energy functional (3.28). In our sharp-interface functional (3.28), the elastic energy $|\boldsymbol{\nabla}\mathbf{Q}|^2$, bulk energy $\bar{F}_b(\mathbf{Q})$, and surface energy are led by coefficients $O(\lambda^{-1})$, $O(\lambda)$, and $O(1)$, respectively, so they influence the final shape of the droplet differently as λ changes. When λ is small, the dominant term is the elastic energy, so $\mathbf{Q}$ tends to become a harmonic function inside the droplet. The zeros of $\mathbf{Q}$ constitute the nematic defects. When λ is large, the dominant term is the bulk energy, so $\mathbf{Q}$ tends to minimize $\bar{F}_b$ and falls into the uniaxial minimizers (2.7). As a side effect, defects are not likely to exist in the stable configuration. On the other hand, the temperature a affects the bulk energy (2.6) by preferring uniaxial $\mathbf{Q}$-tensors, so the tactoid configuration becomes the global minimizer when a is low.

6. Conclusion. In this paper, we propose an improved diffuse-interface LdG model (2.1) for an NLC droplet. We prove the existence of its minimizers and a sharp-interface limit as $\varepsilon \to 0$ (Proposition 3.3). Another Γ-limit where $\kappa \to 0$ is taken (Proposition 3.4) such that the final sharp-interface limit (3.28) complies to the standard droplet energy expression in (1.1), with physically interpretable body energy (3.56) and surface energy (3.57). Then, we apply a heuristic asymptotic analysis to the model and obtain the 1D solutions ((4.12), (4.16), and (4.24)), which illustrate the phenomenon of sharp phase separation at spatial scales ε and κ for ϕ and $\mathbf{Q}$, respectively, as well as the influence of the boundary anchoring coefficient ω on the alignment to the planar anchoring condition (in Figure 4.1(b)).

We also conduct numerical experiments on (2.1) and predict several experimentally and theoretically relevant nematic droplet configurations [38, 25], such as the radial, ring, and tactoid configurations. The tactoid matches experiments well [28]. Additionally, we study the aforementioned configurations under different length scales (Figure 5.1), the results of which show the complex interplay between the topological defects and the droplet shapes. For example, the disclination line pushes the droplet boundary away from the center in the ring configuration, and the pointy ends in a tactoid shove the defects out of the droplet. Finally, we present a schematic phase diagram in Figure 5.2(b) showing the structures of (meta)stable configurations at different values of A, λ. It demonstrates that biaxial configurations (ring and radial) are stable at small sizes λ and high temperature a, and vice versa for the uniaxial tactoid.

Our work provides several directions for future research. First, the interplay between droplet boundaries and internal defect structures could be further investigated by prescribing droplet shapes via the phase field function, thereby enabling control of defect patterns through tailored geometric confinement. Second, our diffuse-interface modelling approach could also be extended to more complex LC droplets such as the smectic phase, of which many observations have been made in experiments (see, e.g., [42, 63]), but mathematical studies remain limited [40]. Furthermore, the integration of our energy functional with dynamic $\mathbf{Q}$-tensor theories offers a feasible approach for investigating the rich temporal behaviors for NLC droplets [44]. This approach could be also adapted to investigate active liquid crystal systems, where the incorporation of energy input leads to fascinating nonequilibrium phenomena.

REFERENCES

[1] J. H. Adler, A. S. Andrei, and T. J. Atherton, *Nonlinear methods for shape optimization problems in liquid crystal tactoids*, Comput. Math. Appl., 187 (2025), pp. 231–248, https://doi.org/10.1016/j.camwa.2025.04.004.

[2] G. Bouchitte, *Singular perturbations of variational problems arising from a two-phase transition model*, Appl. Math. Optim., 21 (1990), pp. 289–314, https://doi.org/10.1007/BF01445167.

[3] K. A. Brakke, *The Surface Evolver*, Exp. Math., 1 (1992), pp. 141–165, https://doi.org/10.1080/10586458.1992.10504253.

[4] J. W. Cahn and J. E. Hilliard, *Free energy of a nonuniform system.* I. *Interfacial free energy*, J. Chem. Phys., 28 (1958), pp. 258–267, https://doi.org/10.1063/1.1744102.

[5] S. Dai, B. Li, and J. Lu, *Convergence of phase-field free energy and boundary force for molecular solvation*, Arch. Ration. Mech. Anal., 227 (2018), pp. 105–147, https://doi.org/10.1007/s00205-017-1158-4.

[6] P. G. de Gennes and J. Prost, *The Physics of Liquid Crystals*, 2nd ed., Oxford Sci. Publ. 83, Clarendon Press, Oxford University Press, Oxford, New York, 1993.

[7] E. De Giorgi, *Convergence problems for functionals and operators*, in Proceedings of the International Meeting on Recent Methods in Nonlinear Analysis (Rome, 1978), Pitagora Editrice, Bologna, 1979, pp. 131–188.

[8] A. DeBenedictis and T. J. Atherton, *Shape minimisation problems in liquid crystals*, Liq. Cryst., 43 (2016), pp. 2352–2362, https://doi.org/10.1080/02678292.2016.1209699.

[9] J. W. Doane, A. Golemme, J. L. West, J. B. Whitehead, and B.-G. Wu, *Polymer dispersed liquid crystals for display application*, Mol. Cryst. Liq. Cryst. Inc. Nonlinear Opt., 165 (1988), pp. 511–532, https://doi.org/10.1080/00268948808082211.

[10] J. L. Ericksen, *Equilibrium theory of liquid crystals*, in Advances in Liquid Crystals, Vol. 2, Elsevier, 1976, pp. 233–298, https://doi.org/10.1016/B978-0-12-025002-8.50012-9.

[11] L. C. Evans, *Partial Differential Equations*, 2nd ed., Grad. Stud. Math. 19, American Mathematical Society, Providence, RI, 2010.

[12] L. C. Evans and R. F. Gariepy, *Measure Theory and Fine Properties of Functions*, rev. ed., Textb. Math., CRC Press, Boca Raton, FL, 2015.

[13] L. C. Evans, H. M. Soner, and P. E. Souganidis, *Phase transitions and generalized motion by mean curvature*, Comm. Pure Appl. Math., 45 (1992), pp. 1097–1123, https://doi.org/10.1002/cpa.3160450903.

[14] L. C. Evans and J. Spruck, *Motion of level sets by mean curvature*, I, J. Differential Geom., 33 (1991), pp. 635–681, https://doi.org/10.4310/jdg/1214446559.

[15] M. G. Forest, Q. Wang, and X. Yang, *LCP droplet dispersions: A two-phase, diffuse-interface kinetic theory and global droplet defect predictions*, Soft Matter, 8 (2012), pp. 9642–9660, https://doi.org/10.1039/c2sm25512j.

[16] F. C. Frank, I. *Liquid crystals. On the theory of liquid crystals*, Discuss. Faraday Soc., 25 (1958), pp. 19–28, https://doi.org/10.1039/df9582500019.

[17] H. Garcke, C. Hecht, M. Hinze, and C. Kahle, *Numerical approximation of phase field based shape and topology optimization for fluids*, SIAM J. Sci. Comput., 37 (2015), pp. A1846–A1871, https://doi.org/10.1137/140969269.

[18] Z. Geng and F. Lin, *The two-dimensional liquid crystal droplet problem with a tangential boundary condition*, Arch. Ration. Mech. Anal., 243 (2022), pp. 1181–1221, https://doi.org/10.1007/s00205-021-01733-5.

[19] Z. Geng, A. Roy, and A. Zarnescu, *Global existence of weak solutions for a model of nematic liquid crystal-colloidal interactions*, SIAM J. Math. Anal., 56 (2024), pp. 4324–4355, https://doi.org/10.1137/23M161149X.

[20] D. Gilbarg and N. S. Trudinger, *Elliptic Partial Differential Equations of Second Order*, Grundlehren der mathematischen Wissenschaften 224, Springer, Berlin, Heidelberg, 1977, https://doi.org/10.1007/978-3-642-96379-7.

[21] E. Giusti, *Minimal Surfaces and Functions of Bounded Variation*, Birkhäuser Boston, Boston, MA, 1984, https://doi.org/10.1007/978-1-4684-9486-0.

[22] D. Golovaty, P. Sternberg, and R. Venkatraman, *A Ginzburg–Landau-type problem for highly anisotropic nematic liquid crystals*, SIAM J. Math. Anal., 51 (2019), pp. 276–320, https://doi.org/10.1137/18M1178360.

[23] J. Han, Y. Luo, W. Wang, P. Zhang, and Z. Zhang, *From microscopic theory to macroscopic theory: A systematic study on modeling for liquid crystals*, Arch. Ration. Mech. Anal., 215 (2015), pp. 741–809, https://doi.org/10.1007/s00205-014-0792-3.

[24] Y. Han, A. Majumdar, and L. Zhang, *A reduced study for nematic equilibria on two-dimensional polygons*, SIAM J. Appl. Math., 80 (2020), pp. 1678–1703, https://doi.org/10.1137/19M1293156.

[25] Y. Hu, Y. Qu, and P. Zhang, *On the disclination lines of nematic liquid crystals*, Commun. Comput. Phys., 19 (2016), pp. 354–379, https://doi.org/10.4208/cicp.210115.180515a.

[26] V. Jamali, N. Behabtu, B. Senyuk, J. A. Lee, I. I. Smalyukh, P. van der Schoot, and M. Pasquali, *Experimental realization of crossover in shape and director field of nematic tactoids*, Phys. Rev. E, 91 (2015), 042507, https://doi.org/10.1103/PhysRevE.91.042507.

[27] A. V. Kaznacheev, M. M. Bogdanov, and A. S. Sonin, *The influence of anchoring energy on the prolate shape of tactoids in lyotropic inorganic liquid crystals*, J. Exp. Theoret. Phys., 97 (2003), pp. 1159–1167, https://doi.org/10.1134/1.1641899.

[28] Y.-K. Kim, S. V. Shiyanovskii, and O. D. Lavrentovich, *Morphogenesis of defects and tactoids during isotropic-nematic phase transition in self-assembled lyotropic chromonic liquid crystals*, J. Phys. Condens. Matter, 25 (2013), 404202, https://doi.org/10.1088/0953-8984/25/40/404202.

[29] S. Kitson and A. Geisow, *Controllable alignment of nematic liquid crystals around microscopic posts: Stabilization of multiple states*, Appl. Phys. Lett., 80 (2002), pp. 3635–3637, https://doi.org/10.1063/1.1478778.

[30] A. V. Knyazev, *Toward the optimal preconditioned eigensolver: Locally optimal block preconditioned conjugate gradient method*, SIAM J. Sci. Comput., 23 (2001), pp. 517–541, https://doi.org/10.1137/S1064827500366124.

[31] S. Kralj, E. G. Virga, and S. Žumer, *Biaxial torus around nematic point defects*, Phys. Rev. E, 60 (1999), pp. 1858–1866, https://doi.org/10.1103/PhysRevE.60.1858.

[32] M. Leoni, O. V. Manyuhina, M. J. Bowick, and M. C. Marchetti, *Defect driven shapes in nematic droplets: Analogies with cell division*, Soft Matter, 13 (2017), pp. 1257–1266, https://doi.org/10.1039/C6SM02584F.

[33] J. Li, M. Forest, Q. Wang, and R. Zhou, *A kinetic theory and benchmark predictions for polymer-dispersed, semi-flexible macromolecular rods or platelets*, Phys. D, 240 (2011), pp. 114–130, https://doi.org/10.1016/j.physd.2010.10.008.

[34] F. Lin and C. C. Poon, *On nematic liquid crystal droplets*, in Elliptic and Parabolic Methods in Geometry, 1st ed., A K Peters/CRC Press, 1996, pp. 91–121, https://doi.org/10.1201/9781439864517.

[35] A. Majumdar, *Equilibrium order parameters of nematic liquid crystals in the Landau-de Gennes theory*, European J. Appl. Math., 21 (2010), pp. 181–203, https://doi.org/10.1017/S0956792509990210.

[36] Y. Maroudas-Sacks, L. Garion, L. Shani-Zerbib, A. Livshits, E. Braun, and K. Keren, *Topological defects in the nematic order of actin fibres as organization centres of Hydra morphogenesis*, Nat. Phys., 17 (2021), pp. 251–259, https://doi.org/10.1038/s41567-020-01083-1.

[37] M. Mata, C. J. García-Cervera, and H. D. Ceniceros, *Ordering kinetics of a conserved binary mixture with a nematic liquid crystal component*, J. Non-Newtonian Fluid Mech., 212 (2014), pp. 18–27, https://doi.org/10.1016/j.jnnfm.2014.08.003.

[38] S. Mkaddem and E. C. Gartland, *Fine structure of defects in radial nematic droplets*, Phys. Rev. E, 62 (2000), pp. 6694–6705, https://doi.org/10.1103/PhysRevE.62.6694.

[39] L. Modica, *The gradient theory of phase transitions and the minimal interface criterion*, Arch. Rational Mech. Anal., 98 (1987), pp. 123–142, https://doi.org/10.1007/BF00251230.

[40] J. A. Moreno-Razo, E. J. Sambriski, N. L. Abbott, J. P. Hernández-Ortiz, and J. J. de Pablo, *Liquid-crystal-mediated self-assembly at nanodroplet interfaces*, Nature, 485 (2012), pp. 86–89, https://doi.org/10.1038/nature11084.

[41] N. J. Mottram and C. J. P. Newton, *Introduction to Q-tensor Theory*, preprint, http://arxiv.org/abs/1409.3542, 2014.

[42] N. Murazawa, S. Juodkazis, and H. Misawa, *Laser manipulation of a smectic liquid-crystal droplet*, European Phys. J. E, 20 (2006), pp. 435–439, https://doi.org/10.1140/epje/i2006-10033-1.

[43] Y. A. Nastishin, H. Liu, T. Schneider, V. Nazarenko, R. Vasyuta, S. V. Shiyanovskii, and O. D. Lavrentovich, *Optical characterization of the nematic lyotropic chromonic liquid crystals: Light absorption, birefringence, and scalar order parameter*, Phys. Rev. E, 72 (2005), 041711, https://doi.org/10.1103/PhysRevE.72.041711.

[44] G. Negro, L. C. Head, L. N. Carenza, T. N. Shendruk, D. Marenduzzo, G. Gonnella, and A. Tiribocchi, *Topology controls flow patterns in active double emulsions*, Nat. Commun., 16 (2025), 1412, https://doi.org/10.1038/s41467-025-56236-8.

[45] L. Onsager, *The effects of shape on the interaction of colloidal particles*, Ann. New York Acad. Sci., 51 (1949), pp. 627–659, https://doi.org/10.1111/j.1749-6632.1949.tb27296.x.

[46] C. W. Oseen, *The theory of liquid crystals*, Trans. Faraday Soc., 29 (1933), 883–899, https://doi.org/10.1039/tf9332900883.

[47] S. Osher and R. Fedkiw, *Level Set Methods and Dynamic Implicit Surfaces*, Appl. Math. Sci. 153, Springer, New York, 2003, https://doi.org/10.1007/b98879.

[48] Y. Sawa, K. Urayama, T. Takigawa, V. Gimenez-Pinto, B. L. Mbanga, F. Ye, J. V. Selinger, and R. L. B. Selinger, *Shape and chirality transitions in off-axis twist nematic elastomer ribbons*, Phys. Rev. E, 88 (2013), 022502, https://doi.org/10.1103/PhysRevE.88.022502.

[49] B. Shi, Y. Han, A. Majumdar, and L. Zhang, *Multistability for nematic liquid crystals in cuboids with degenerate planar boundary conditions*, SIAM J. Appl. Math., 84 (2024), pp. 756–781, https://doi.org/10.1137/23M1604606.

[50] B. Shi, Y. Han, J. Yin, A. Majumdar, and L. Zhang, *Hierarchies of critical points of a Landau-de Gennes free energy on three-dimensional cuboids*, Nonlinearity, 36 (2023), pp. 2631–2654, https://doi.org/10.1088/1361-6544/acc62d.

[51] A. A. Sonin, *Pierre-Gilles de Gennes and physics of liquid crystals*, Liq. Cryst. Rev., 6 (2018), pp. 109–128, https://doi.org/10.1080/21680396.2018.1474813.

[52] T. J. Spencer, C. M. Care, R. M. Amos, and J. C. Jones, *Zenithal bistable device: Comparison of modeling and experiment*, Phys. Rev. E, 82 (2010), 021702, https://doi.org/10.1103/PhysRevE.82.021702.

[53] P. Sternberg, *The effect of a singular perturbation on nonconvex variational problems*, Arch. Rational Mech. Anal., 101 (1988), pp. 209–260, https://doi.org/10.1007/BF00253122.

[54] A. K. Tarafder, A. von Kügelgen, A. J. Mellul, U. Schulze, D. G. A. L. Aarts, and T. A. M. Bharat, *Phage liquid crystalline droplets form occlusive sheaths that encapsulate and protect infectious rod-shaped bacteria*, Proc. Natl. Acad. Sci., 117 (2020), pp. 4724–4731, https://doi.org/10.1073/pnas.1917726117.

[55] L. Tortora and O. D. Lavrentovich, *Chiral symmetry breaking by spatial confinement in tactoidal droplets of lyotropic chromonic liquid crystals*, Proc. Natl. Acad. Sci., 108 (2011), pp. 5163–5168, https://doi.org/10.1073/pnas.1100087108.

[56] L. Tortora, H.-S. Park, S.-W. Kang, V. Savaryn, S.-H. Hong, K. Kaznatcheev, D. Finotello, S. Sprunt, S. Kumar, and O. D. Lavrentovich, *Self-assembly, condensation, and order in aqueous lyotropic chromonic liquid crystals crowded with additives*, Soft Matter, 6 (2010), 4157–4167, https://doi.org/10.1039/c0sm00065e.

[57] J. D. van der Waals, *The thermodynamic theory of capillarity under the hypothesis of a continuous variation of density*, J. Stat. Phys., 20 (1979), pp. 200–244, https://doi.org/10.1007/BF01011514.

[58] E. G. Virga, *Drops of nematic liquid crystals*, Arch. Rational Mech. Anal., 107 (1989), pp. 371–390, https://doi.org/10.1007/BF00251555.

[59] E. G. Virga, *Variational Theories for Liquid Crystals*, Appl. Math. Math. Comput. 8, 1st ed., Chapman & Hall, London, Weinheim, 1994.

[60] P.-X. Wang and M. J. MacLachlan, *Liquid crystalline tactoids: Ordered structure, defective coalescence and evolution in confined geometries*, Philos. Trans. Roy. Soc. A, 376 (2018), 20170042, https://doi.org/10.1098/rsta.2017.0042.

[61] W. Wang, L. Zhang, and P. Zhang, *Modelling and computation of liquid crystals*, Acta Numer., 30 (2021), pp. 765–851, https://doi.org/10.1017/S0962492921000088.

[62] Y. Wang and J. Li, *Phase field modeling of defects and deformation*, Acta Mater., 58 (2010), pp. 1212–1235, https://doi.org/10.1016/j.actamat.2009.10.041.

[63] W.-S. Wei, J. Jeong, P. J. Collings, and A. G. Yodh, *Focal conic flowers, dislocation rings, and undulation textures in smectic liquid crystal Janus droplets*, Soft Matter, 18 (2022), pp. 4360–4371, https://doi.org/10.1039/D1SM01623G.

[64] J. L. West, *Phase separation of liquid crystals in polymers*, Mol. Cryst. Liq. Cryst. Inc. Nonlinear Opt., 157 (1988), pp. 427–441, https://doi.org/10.1080/00268948808080247.

[65] D. Wu, B. Shi, Y. Han, P. Zhang, A. Majumdar, and L. Zhang, *A diffuse-interface Landau–de Gennes model for free boundary problems in the theory of nematic liquid crystals*, SIAM J. Math. Anal., 57 (2025), pp. 4358–4395, https://doi.org/10.1137/24M1710322.

[66] G. Wulff, XXV. *Zur Frage der Geschwindigkeit des Wachsthums und der Auflösung der Krystallflächen*, Zeitschrift für Kristallographie - Crystalline Materials, 34 (1901), pp. 449–530, https://doi.org/10.1524/zkri.1901.34.1.449.

[67] X. Xing, H. Shin, M. J. Bowick, Z. Yao, L. Jia, and M.-H. Li, *Morphology of nematic and smectic vesicles*, Proc. Natl. Acad. Sci., 109 (2012), pp. 5202–5206, https://doi.org/10.1073/pnas.1115684109.

[68] P. Yue, J. J. Feng, C. Liu, and J. Shen, *A diffuse-interface method for simulating two-phase flows of complex fluids*, J. Fluid Mech., 515 (2004), pp. 293–317, https://doi.org/10.1017/S0022112004000370.

[69] D. C. Zografopoulos, R. Beccherelli, and E. E. Kriezis, *Beam-splitter switches based on zenithal bistable liquid-crystal gratings*, Phys. Rev. E, 90 (2014), 042503, https://doi.org/10.1103/PhysRevE.90.042503.